



UNIVERSITY  
of  
GREENWICH

**Greenwich Academic Literature Archive (GALA)**  
– the University of Greenwich open access repository  
<http://gala.gre.ac.uk>

---

*Citation for published version:*

Terrana, S., Nguyen, N.C. ORCID: 0000-0001-9167-5780, Bonet, J. ORCID: 0000-0002-0430-5181 and Peraire, J. (2019) A hybridizable discontinuous Galerkin method for both thin and 3D nonlinear elastic structures. *Computer Methods in Applied Mechanics and Engineering*, 352. pp. 561-585. ISSN 0045-7825 (doi:<https://doi.org/10.1016/j.cma.2019.04.029>)

*Publisher's version available at:*

<https://dx.doi.org/10.1016/j.cma.2019.04.029>

---

**Please note that where the full text version provided on GALA is not the final published version, the version made available will be the most up-to-date full-text (post-print) version as provided by the author(s). Where possible, or if citing, it is recommended that the publisher's (definitive) version be consulted to ensure any subsequent changes to the text are noted.**

*Citation for this version held on GALA:*

Terrana, S., Nguyen, N.C., Bonet, J. and Peraire, J. (2019) A hybridizable discontinuous Galerkin method for both thin and 3D nonlinear elastic structures. London: Greenwich Academic Literature Archive.

Available at: <http://gala.gre.ac.uk/id/eprint/23898/>

---

Contact: [gala@gre.ac.uk](mailto:gala@gre.ac.uk)

## Accepted Manuscript

A hybridizable discontinuous Galerkin method for both thin and 3D nonlinear elastic structures

S. Terrana, N.C. Nguyen, J. Bonet, J. Peraire



PII: S0045-7825(19)30232-4  
DOI: <https://doi.org/10.1016/j.cma.2019.04.029>  
Reference: CMA 12417

To appear in: *Comput. Methods Appl. Mech. Engrg.*

Received date : 23 December 2018  
Revised date : 19 April 2019  
Accepted date : 24 April 2019

Please cite this article as: S. Terrana, N.C. Nguyen, J. Bonet et al., A hybridizable discontinuous Galerkin method for both thin and 3D nonlinear elastic structures, *Computer Methods in Applied Mechanics and Engineering* (2019), <https://doi.org/10.1016/j.cma.2019.04.029>

This is a PDF file of an unedited manuscript that has been accepted for publication. As a service to our customers we are providing this early version of the manuscript. The manuscript will undergo copyediting, typesetting, and review of the resulting proof before it is published in its final form. Please note that during the production process errors may be discovered which could affect the content, and all legal disclaimers that apply to the journal pertain.

- We present a hybridizable discontinuous Galerkin (HDG) method for thin and thick structures at finite deformations
- A technique of elimination of unknowns for thin structures significantly reduces the computational cost
- We present an empirical penalization that both alleviates the locking effects and stabilizes the HDG method
- The optimal convergence is achieved for the displacement and an extra half-order of convergence can be gained with an inexpensive postprocessing
- The method gives accurate results for various classical nonlinear shell problems

# A hybridizable discontinuous Galerkin method for both thin and 3D nonlinear elastic structures

S. Terrana<sup>a,\*</sup>, N.C. Nguyen<sup>a</sup>, J. Bonet<sup>b</sup>, J. Peraire

<sup>a</sup>Massachusetts Institute of Technology, 77 Massachusetts Ave, Cambridge, MA 02139, USA

<sup>b</sup>University of Greenwich, London, SE10 9LS, United Kingdom

---

## Abstract

We present a 3D hybridizable discontinuous Galerkin (HDG) method for nonlinear elasticity which can be efficiently used for thin structures with large deformation. The HDG method is developed for a three-field formulation of nonlinear elasticity and is endowed with a number of attractive features that make it ideally suited for thin structures. Regarding robustness, the method avoids a variety of locking phenomena such as membrane locking, shear locking, and volumetric locking. Regarding accuracy, the method yields *optimal convergence* for the displacements, which can be further improved by an inexpensive postprocessing. And finally, regarding efficiency, the only globally coupled unknowns are the degrees of freedom of the numerical trace on the *interior faces*, resulting in substantial savings in computational time and memory storage. This last feature is particularly advantageous for thin structures because the number of interior faces is typically small. In addition, we discuss the implementation of the HDG method with arc-length algorithms for phenomena such as snap-through, where the standard load incrementation algorithm becomes unstable. Numerical results are presented to verify the convergence and demonstrate the performance of the HDG method through simple analytical and popular benchmark problems in the literature.

**Keywords:** Shell structures, Discontinuous Galerkin method, Nonlinear

---

\*Corresponding author

Email address: [terrana@mit.edu](mailto:terrana@mit.edu) (S. Terrana)

1  
2  
3  
4  
5  
6  
7  
8  
9 elasticity, Superconvergence, Finite element, Hybridizable discontinuous  
10 Galerkin  
11

---

## 12 13 1. Introduction

14  
15  
16 The discontinuous Galerkin (DG) method has been proven to be a valuable  
17 and versatile tool for numerical analysis in continuum mechanics, see e.g. [1, 2,  
18 3]. In solid mechanics, DG methods have been proposed for linear elasticity (see  
19 [4] among many others), nonlinear hyperelasticity [5, 6–7], as well as plasticity [8,  
20 9].

21  
22  
23 However, DG methods have been often criticized for having to employ sig-  
24 nificantly more degrees of freedom than more standard continuous Galerkin  
25 (CG) methods. Hybridizable discontinuous Galerkin (HDG) methods have sub-  
26 sequently been developed to address this drawback. The advantage of HDG  
27 methods is twofold. First, HDG methods parametrize the finite element solution  
28 in terms of an approximation of the displacement on the element boundaries, the  
29 so-called *hybrid* field. Therefore, the only globally coupled unknowns are those  
30 corresponding to the hybrid field, which is unique for the two elements sharing  
31 a boundary. As a consequence, the global linear system to be solved is smaller  
32 than that obtained with the original DG degrees of freedom (DoF). Second,  
33 when polynomials of degree  $k$  are used to approximate both the displacement  
34 and its gradient, both approximations converge with the optimal order  $k + 1$ .  
35 Then, provided  $k \geq 1$ , an elementwise post-processing step can be performed to  
36 obtain a superconvergent solution of order  $k + 2$  for the displacement. HDG ap-  
37 proaches have been developed for both linear elasticity [10, 11, 12, 13, 14] and  
38 nonlinear elasticity [15, 11, 16, 17, 18]. Although the superconvergence has  
39 been often observed with these HDG approaches, it is not guaranteed in general  
40 for elasticity [13]. This paper proposes an extension of the HDG volumetric  
41 methods for nonlinear elasticity to thin structures.

42  
43  
44 Traditionally, thin structures have been modeled using special elements, as  
45 it is well known that classical low order finite elements fail to model such struc-  
46  
47  
48  
49  
50  
51  
52  
53  
54  
55  
56  
57  
58  
59  
60  
61  
62  
63  
64  
65

1  
2  
3  
4  
5  
6  
7  
8  
9  
10  
11  
12  
13  
14  
15  
16  
17  
18  
19  
20  
21  
22  
23  
24  
25  
26  
27  
28  
29  
30  
31  
32  
33  
34  
35  
36  
37  
38  
39  
40  
41  
42  
43  
44  
45  
46  
47  
48  
49  
50  
51  
52  
53  
54  
55  
56  
57  
58  
59  
60  
61  
62  
63  
64  
65

tures, due to several locking effects. Special plate and shell finite elements has been developed over the past fifty years, either based on a plate/shell theories, or by simplifying three-dimensional continuum theories (see reviews in [19, 20, 21], and in particular [22, 23, 24] for DG approaches). Both approaches have been shown to model accurately finite deformations of thin structures. However, they suffer from common disadvantages and difficulties. Among these difficulties are the coupling with solid finite elements (rotational degrees of freedom have to be connected with the solid element displacements using special transition elements), the application of particular boundary conditions, the complex updates of rotation vectors for large deformations, and the difficult degeneration of full 3D constitutive laws. Finally, the objectivity of the strain measures may be lost (see [25]). In order to overcome these drawbacks, alternative low-order solid-shell elements have been then developed (see [26, 27, 28, 29, 30] among many others), able to model both thick and thin structures. These elements are volumetric solid bricks modified with a variety of techniques in order to tame the locking pathologies. Among these techniques, the reduced integration [31, 32, 33] and the B-bar [34–35] approaches address mainly the volumetric locking. The enhanced strain technique prevents volumetric [36] and membrane lockings [37] – see also [38, 29, 39, 40]. And coming from plate [41] and shell elements [42], the assumed natural strain technique can control the shear locking of solid shell elements [28, 27, 43, 39].

The present approach is different and, in many respects, simpler. We directly discretize the thin structures with high-order three dimensional elements and employ a non-linear elasticity HDG volumetric formulation. This approach is motivated by the following observations. As a high-order finite element approach, all the thickness-related locking behaviors should vanish for high enough polynomial degrees [44, 45, 46]. Moreover, even for moderate polynomial degrees, the discontinuous nature of the approximations mitigates the locking effects, as previously observed for both beams [47] and shells [22]. In particular, as a discontinuous Galerkin approach, our method is free from volumetric locking for nearly-incompressible materials [4]. Finally, in our method, the only globally

coupled unknowns are those representing the hybrid field which is defined on the *interior faces* only. This leads to substantial savings in computational time and memory storage for thin structures because the number of interior faces is small.

The article is organized as follows. In Section 2, we introduce the notations used throughout the paper. In Section 3, we introduce the HDG method based on a new variational principle. In Section 4, we discuss the implementation of the HDG method together with loading incrementation, Newton-Raphson, and Arc-Length algorithms. In particular, we explain how to take advantage of the discontinuity of the hybrid field to significantly reduce the size of the global linear system when thin structures are considered. In Section 5, we present numerical results to assess the convergence of the HDG method and its accuracy on several classical non-linear shells benchmark problems. Finally, in Section 6, we provide some concluding remarks.

## 2. Governing equations and notations

### 2.1. Nonlinear elasticity equations

We consider a deformable elastic body, occupying the volume  $\Omega \in \mathbb{R}^d$  in the initial, undeformed configuration. The initial configuration  $\Omega$  is assumed to be an open and bounded polygonal domain with a Lipschitz continuous boundary  $\partial\Omega$ . This boundary is divided into a Dirichlet boundary  $\Gamma_D$  and a Neumann boundary  $\Gamma_N$  such that  $\partial\Omega = \overline{\Gamma_D \cup \Gamma_N}$  and  $\Gamma_D \cap \Gamma_N = \emptyset$ . The material position vector is denoted  $\varphi(\mathbf{X})$ , with  $\mathbf{X}$  denoting the reference material coordinates. Under given body forces  $\mathbf{f}$ , prescribed tractions  $\mathbf{t}$  on  $\Gamma_N$ , and prescribed displacements  $\mathbf{u}_D$  on  $\Gamma_D$ , the elastic body undergoes a deformation satisfying the

following static equilibrium equations

$$-\nabla \cdot \mathbf{P} = \mathbf{f} \quad \text{in } \Omega \quad (1a)$$

$$\mathbf{F} - \nabla \varphi = 0 \quad \text{in } \Omega, \quad (1b)$$

$$\mathbf{P} - \frac{\partial \Psi}{\partial \mathbf{F}} = 0 \quad \text{in } \Omega, \quad (1c)$$

$$\varphi = \varphi_D, \quad \text{on } \Gamma_D. \quad (1d)$$

$$\mathbf{P}\mathbf{N} = \mathbf{t} \quad \text{on } \Gamma_N. \quad (1e)$$

Here,  $\mathbf{F}$  is the deformation gradient and  $\mathbf{P}$  is the first Piola-Kirchhoff stress tensor. The gradient  $\nabla$ , and the divergence  $\nabla \cdot$  operators are defined with respect to the initial (undeformed) material coordinate system. And  $\mathbf{N}$  is the outward normal on the undeformed body surface. We assume that the material properties, applied loads and boundary conditions are sufficiently smooth.

We limit the scope of this article to hyperelastic materials. In particular, we assume that an elastic potential energy function  $\Psi(\mathbf{F})$  exists as a function of the deformation gradient, and that it is related to the first Piola-Kirchhoff stress tensors through the relation (1c).

For the applications considered in this paper, only the Saint Venant-Kirchhoff and the Neo-Hookean hyperelastic models will be considered. Their respective elastic potential functions are given by

$$\Psi(\mathbf{F}) = \frac{\lambda}{2} (\text{tr } \mathbf{E})^2 + \mu \text{tr}(\mathbf{E}^2) \quad \text{Saint Venant-Kirchhoff} \quad (2a)$$

$$\Psi(\mathbf{F}) = \frac{\mu}{2} (\text{tr}(\mathbf{E}^T \mathbf{E}) - 3 - 2 \ln J) + \frac{\lambda}{2} (\ln J)^2 \quad \text{Neo-Hookean} \quad (2b)$$

where  $(\lambda, \mu)$  are Lamé parameters of the model,  $J = \det \mathbf{F}$  is the the Jacobian,  $\mathbf{E} = \frac{1}{2}(\mathbf{F}^T \mathbf{F} - \mathbf{I})$  is the Lagrangian strain tensor, and  $\mathbf{I}$  the second order identity tensor.

## 2.2 Approximation spaces

We assume that  $\Omega$  is divided into a partition  $\mathcal{T}_h$  of disjoint elements  $K$ , and introduce the set  $\partial \mathcal{T}_h = \{\partial K : K \in \mathcal{T}_h\}$ , the set of internal faces  $\mathcal{E}_h^o =$



90  $\{\partial K_i \cap \partial K_j : K_i, K_j \in \mathcal{T}_h\}$ , the set of boundary faces  $\mathcal{E}_h^\partial = \{\partial K_i \cap \Omega : K_i \in \mathcal{T}_h\}$ ,  
and set of all faces  $\mathcal{E}_h = \mathcal{E}_h^\circ \cup \mathcal{E}_h^\partial$ .

We denote by  $\mathcal{P}_k(K)$  the set of polynomials of degree at most  $k$  whose support is the element  $K$ , and introduce the following broken polynomial spaces

$$\mathbf{V}_h := \{\mathbf{G} \in [L^2(\Omega)]^{d \times d} : \mathbf{G}|_K \in [\mathcal{P}_k(L)]^{d \times d}, \forall K \in \mathcal{T}_h\}, \quad (3a)$$

$$\mathbf{W}_h := \{\mathbf{w} \in L^2(\Omega)^d : \mathbf{w}|_K \in \mathcal{P}_k(K)^d, \forall K \in \mathcal{T}_h\}, \quad (3b)$$

$$\mathbf{M}_h := \{\boldsymbol{\mu} \in L^2(\mathcal{E}_h)^d : \boldsymbol{\mu}|_F \in \mathcal{P}_k(F), \forall F \in \mathcal{E}_h\}, \quad (3c)$$

where  $L^2(D)$  is the space of square integrable functions on  $D$ . We have chosen equal polynomial degrees for vector, tensor and trace spaces. However, the HDG framework is quite general and, in principle, it allows for other approximation  
95 spaces such as the Raviart-Thomas and the Brezzi-Douglas-Marini spaces as noted in [48, 49].

Finally, we define various inner products for our finite element spaces

$$\begin{aligned} (\mathbf{u}, \mathbf{v})_K &:= \int_K \mathbf{u} \cdot \mathbf{v} \, d\Omega, & (\mathbf{u}, \mathbf{v})_{\mathcal{T}_h} &:= \sum_{K \in \mathcal{T}_h} (\mathbf{u}, \mathbf{v})_K, & \forall \mathbf{u}, \mathbf{v} \in L^2(\Omega)^d, \\ (\mathbf{G}, \mathbf{H})_K &:= \int_K \mathbf{G} : \mathbf{H} \, d\Omega, & (\mathbf{G}, \mathbf{H})_{\mathcal{T}_h} &:= \sum_{K \in \mathcal{T}_h} (\mathbf{G}, \mathbf{H})_K, & \forall \mathbf{G}, \mathbf{H} \in L^2(\Omega)^{d \times d}, \\ \langle \boldsymbol{\mu}, \boldsymbol{\eta} \rangle_{\partial K} &:= \int_{\partial K} \boldsymbol{\mu} \cdot \boldsymbol{\eta} \, d\Gamma, & \langle \boldsymbol{\mu}, \boldsymbol{\eta} \rangle_{\partial \mathcal{T}_h} &:= \sum_{K \in \mathcal{T}_h} \langle \boldsymbol{\mu}, \boldsymbol{\eta} \rangle_{\partial K}, & \forall \boldsymbol{\mu}, \boldsymbol{\eta} \in L^2(\partial \mathcal{T}_h)^d. \end{aligned}$$

In the next section, we will define the HDG method for solving the problem (1).

### 3. Hybridizable discontinuous Galerkin formulation

#### 3.1. Variational principle

100 As explained in [16], the HDG method for nonlinear elasticity can be seen as a minimization problem of an energy functional. The functional proposed therein is a function of the deformation  $\boldsymbol{\varphi}$  and the deformation traces  $\hat{\boldsymbol{\varphi}} := \boldsymbol{\varphi}|_{\mathcal{E}_h}$ , with the deformation gradient being retrieved via the use of the DG-derivative [5, 16].

We present here an alternative 4-variables variational principle that can be used  
 105 to derive the same HDG equations, without making use of the DDC-derivative.

This variational principle is associated to the following functional defined for  
 fields  $(\varphi, \mathbf{P}, \mathbf{F}, \hat{\varphi}) \in \mathbf{W}_h \times \mathbf{V}_h \times \mathbf{V}_h \times \mathbf{M}_h$ ,

$$\begin{aligned} \Pi(\varphi, \mathbf{P}, \mathbf{F}, \hat{\varphi}) := & (\Psi(\mathbf{F}), 1)_{\mathcal{T}_h} + (\mathbf{P}, (\nabla\varphi - \mathbf{F}))_{\mathcal{T}_h} \\ & - \langle \mathbf{PN}, (\varphi - \hat{\varphi}) \rangle_{\partial\mathcal{T}_h} + \frac{1}{2} \langle (\varphi - \hat{\varphi}), \boldsymbol{\tau}(\varphi - \hat{\varphi}) \rangle_{\partial\mathcal{T}_h} \quad (5) \\ & - \langle \mathbf{f}, \varphi \rangle_{\mathcal{T}_h} - \langle \mathbf{t}, \hat{\varphi} \rangle_{\Gamma_N} + \frac{1}{2} \langle (\hat{\varphi} - \varphi_D), \boldsymbol{\tau}(\hat{\varphi} - \varphi_D) \rangle_{\Gamma_D}, \end{aligned}$$

where  $\boldsymbol{\tau}$  is the stabilization matrix. The first term on the right hand side corre-  
 sponds to the internal energy of the elastic body, the second measures an energy  
 110 associated to the mismatch between  $\nabla\varphi$  and  $\mathbf{F}$ . The third and fourth terms  
 measure an energy related to the jump of the solution at the elements bound-  
 aries. In particular, the fourth term is typical of the HDG formulation. As an  
 energy quantity, it has to be positive i.e. the matrix  $\boldsymbol{\tau}$  has to be symmetric def-  
 inite positive. The choice of  $\boldsymbol{\tau}$  crucially affects the performances of the method  
 115 (see discussion in 3.3). The fifth term is the energy related with the external  
 body forces. Finally, the last two terms are the energies associated with the  
 imposed tractions and displacements. Although the Dirichlet boundary condi-  
 tion is applied weakly here, it could be applied alternatively in a strong manner  
 through a suitable modification of the space  $\mathbf{M}_h$ .

120 Interestingly, the variational principle (5) becomes the Hu-Washizu principle  
 when  $\hat{\varphi} \equiv \varphi$  on  $\mathcal{T}_h$ . Moreover, if  $\mathbf{F} \equiv \nabla\varphi$ , it becomes the standard total energy  
 used for continuous Galerkin displacement formulations (see for instance [50]).

We now define the directional derivative of  $\Pi$  with respect to its first variable  
 and in the direction  $\mathbf{w}$  as

$$D_1\Pi(\varphi, \mathbf{P}, \mathbf{F}, \hat{\varphi})[\mathbf{w}] := \left. \frac{\partial}{\partial\epsilon} \Pi(\varphi + \epsilon\mathbf{w}, \mathbf{P}, \mathbf{F}, \hat{\varphi}) \right|_{\epsilon=0}, \quad (6)$$

125 for any  $\mathbf{w} \in \mathbf{W}_h$ . The directional derivatives  $D_2\Pi, D_3\Pi$  and  $D_4\Pi$  with respect  
 to the other variables can be defined in a similar way.

We can now express the HDG equations as a variational principle. The HDG  
 approximation  $(\varphi_h, \mathbf{P}_h, \mathbf{F}_h, \hat{\varphi}_h)$  to the exact solution  $(\varphi, \mathbf{P}, \mathbf{F}, \hat{\varphi})$  is the element

of the approximation space  $\mathbf{W}_h \times \mathbf{V}_h \times \mathbf{V}_h \times \mathbf{M}_h$  that locally minimizes the energy functional  $\Pi$ , that is making all the directional derivatives simultaneously equal to zero.

Thus, for the first directional derivative,  $D_1\Pi = 0$  yields the following HDG approximation

$$(\mathbf{P}_h, (\nabla \mathbf{w}))_{\mathcal{T}_h} - (\mathbf{f}, \mathbf{w})_{\mathcal{T}_h} - \langle \mathbf{P}_h \mathbf{N}, \mathbf{w} \rangle_{\partial \mathcal{T}_h} + \langle \boldsymbol{\tau}(\varphi_h - \hat{\varphi}_h), \mathbf{w} \rangle_{\partial \mathcal{T}_h} = 0, \quad (7)$$

for all  $\mathbf{w} \in \mathbf{W}_h$ . By introducing the numerical traction traces

$$\widehat{\mathbf{P}}_h \mathbf{N} := \mathbf{P}_h \mathbf{N} - \boldsymbol{\tau}(\varphi_h - \hat{\varphi}_h) \quad \text{on } \partial \mathcal{T}_h, \quad (8)$$

we can rewrite (7) as

$$(\mathbf{P}_h, (\nabla \mathbf{w}))_{\mathcal{T}_h} - (\mathbf{f}, \mathbf{w})_{\mathcal{T}_h} - \langle \widehat{\mathbf{P}}_h \mathbf{N}, \mathbf{w} \rangle_{\partial \mathcal{T}_h} = 0, \quad \forall \mathbf{w} \in \mathbf{W}_h. \quad (9)$$

For the second directional derivative, setting  $D_2\Pi = 0$  we get

$$((\nabla \varphi_h - \mathbf{F}_h), \mathbf{G})_{\mathcal{T}_h} - \langle (\varphi_h - \hat{\varphi}_h), \mathbf{G} \mathbf{N} \rangle_{\partial \mathcal{T}_h} = 0, \quad \forall \mathbf{G} \in \mathbf{V}_h,$$

where the gradient term can be integrated by parts to obtain

$$-(\varphi_h, \nabla \cdot \mathbf{G})_{\mathcal{T}_h} - (\varphi_h, \mathbf{G})_{\mathcal{T}_h} + \langle \hat{\varphi}_h, \mathbf{G} \mathbf{N} \rangle_{\partial \mathcal{T}_h} = 0, \quad \forall \mathbf{G} \in \mathbf{V}_h. \quad (10)$$

The vanishing condition for third directional derivative,  $D_3\Pi = 0$ , yields

$$\left( \frac{\partial \Psi(\mathbf{F}_h)}{\partial \mathbf{F}_h} - \mathbf{P}_h, \mathbf{Q} \right)_{\mathcal{T}_h} = 0, \quad \forall \mathbf{Q} \in \mathbf{V}_h. \quad (11)$$

And finally, enforcing  $D_4\Pi = 0$ , we obtain

$$\langle \widehat{\mathbf{P}}_h \mathbf{N}, \boldsymbol{\mu} \rangle_{\partial \mathcal{T}_h} - \langle \mathbf{t}, \boldsymbol{\mu} \rangle_{\Gamma_N} + \langle \boldsymbol{\tau}(\hat{\varphi}_h - \varphi_D), \boldsymbol{\mu} \rangle_{\Gamma_D} = 0, \quad \forall \boldsymbol{\mu} \in \mathbf{M}_h. \quad (12)$$

## 2. Weak formulation

The HDG solution satisfies equations (9), (10), (11) and (12), which we present now in a more customary fashion : the HDG method seeks an approxi-

mation  $(\varphi_h, \mathbf{P}_h, \mathbf{F}_h, \hat{\varphi}_h) \in \mathbf{W}_h \times \mathbf{V}_h \times \mathbf{V}_h \times \mathbf{M}_h$  such that

$$(\mathbf{P}_h, \nabla \mathbf{w})_{\mathcal{T}_h} - \langle \widehat{\mathbf{P}}_h \mathbf{N}, \mathbf{w} \rangle_{\partial \mathcal{T}_h} = (\mathbf{f}, \mathbf{w})_{\mathcal{T}_h} \quad \forall \mathbf{w} \in \mathbf{V}_h, \quad (13a)$$

$$(\mathbf{F}_h, \mathbf{G})_{\mathcal{T}_h} + (\varphi_h, \nabla \cdot \mathbf{G})_{\mathcal{T}_h} - \langle \hat{\varphi}_h, \mathbf{G} \mathbf{N} \rangle_{\partial \mathcal{T}_h} = 0 \quad \forall \mathbf{G} \in \mathbf{V}_h, \quad (13b)$$

$$(\mathbf{P}_h, \mathbf{Q})_{\mathcal{T}_h} - \left( \frac{\partial \Psi}{\partial \mathbf{F}_h}, \mathbf{Q} \right)_{\mathcal{T}_h} = 0 \quad \forall \mathbf{Q} \in \mathbf{V}_h, \quad (13c)$$

$$\langle \widehat{\mathbf{P}}_h \mathbf{N}, \boldsymbol{\mu} \rangle_{\partial \mathcal{T}_h \setminus \Gamma_D} + \langle \boldsymbol{\tau}(\hat{\varphi}_h - \varphi_D), \boldsymbol{\mu} \rangle_{\Gamma_D} = \langle \boldsymbol{\nu}, \boldsymbol{\mu} \rangle_{\Gamma_N} \quad \forall \boldsymbol{\mu} \in \mathbf{M}_h, \quad (13d)$$

140 where the numerical traction traces are

$$\widehat{\mathbf{P}}_h \mathbf{N} := \mathbf{P}_h \mathbf{N} - \boldsymbol{\tau}(\varphi_h - \varphi_n) \quad \text{on } \partial \mathcal{T}_h. \quad (13e)$$

Note that the equation involving the traces (13d), enforce both the boundary conditions (Neumann and Dirichlet) and the jump of  $\widehat{\mathbf{P}}_h \mathbf{N}$  to be zero on the internal faces. This last condition is commonly referred as the *conservativity condition*.

145 The HDG method presented in this article is therefore similar to [15, 16]. It differs from [11] since no approximation of the pressure field as such is made in our formulation.

Although  $\mathbf{F}_h$  and  $\mathbf{P}_h$  are considered here as separate variables,  $\mathbf{P}_h(\mathbf{F}_h)$  can be computed elementwise with equation (13c). Therefore, in the remainder of 150 this paper we will consider only  $(\varphi_h, \mathbf{F}_h, \hat{\varphi}_h)$  as separate variables.

### 3.3. Choice of the stabilization Tensor

The choice of the stabilization tensor  $\boldsymbol{\tau}$  plays a crucial role in both the accuracy and the stability of the method. A very large  $\boldsymbol{\tau}$  means a strong penalization of the inter element discontinuities, in which case the HDG solution becomes 155 very close to a conforming continuous solution. Therefore, for large  $\boldsymbol{\tau}$ , the HDG solution mimics the good and bad properties of conforming methods. Among the good ones, the coercivity is ensured, and hence the stability of the linearized problem. Among the bad ones are the sensitivity of the numerical solution to the chosen mesh and the various locking phenomena (volumetric and thickness-related lockings). In particular, the thickness-related lockings, i.e. shear locking, 160

1  
2  
3  
4  
5  
6  
7  
8  
9 membrane locking and trapezoidal locking are often too severe to make legacy  
10 volumetric finite elements applicable to shell problems. These effects are briefly  
11 illustrated in subsection 5.3.2.  
12

13  
14 On the contrary, for smaller values of the stabilization parameter, the DG-  
15 based methods have shown a better accuracy than their CG counterparts, as  
16 165 allowing jumps of the solution at the elements boundaries provides a mechanism  
17 that significantly mitigates the various locking pathologies. This advantage has  
18 justified the over-cost of the DG-based approximations. However, it comes  
19 with the risk of losing the coercivity of the discrete problem, which translates  
20 into either a non-convergence of the Newton algorithm, or into a converged  
21 non-physical state of deformation (see [16]). Therefore, an ideal  $\tau$  would be  
22 170 into either a non-convergence of the Newton algorithm, or into a converged  
23 non-physical state of deformation (see [16]). Therefore, an ideal  $\tau$  would be  
24 large enough to ensure the stability, while being small enough to retain an  
25 optimal accuracy. How to automatically choose the optimal stabilization is still  
26 a theoretical issue which has been partially addressed in [18] by providing lower  
27 175 bounds for  $\tau$  and for simplex meshes. Although a theoretical estimate of  $\tau$  is  
28 beyond the scope of this paper, we hope to provide some practical insights to  
29 choose an appropriate stabilization.  
30  
31  
32  
33  
34  
35  
36

### 37 3.3.1. Review of some stabilization tensors for nonlinear elasticity

38  
39 Several stabilization strategies have been proposed in the literature for both  
40 180 DG and HDG approaches. However, all of them were found to be of little use  
41 when nonlinear shell problems are solved with HDG. We now briefly review  
42 them and mention what we think are their shortcomings.  
43  
44

45 The simplest approach [11], based on a dimensional analysis is to choose

$$46 \quad \tau = \frac{1}{L_c} \mu \mathbf{I}, \quad (14)$$

47 where  $L_c$  is a length scale that only depends on the discretized geometry of the  
48 185 structure,  $\mu$  the Lamé parameter and  $\mathbf{I}$  the second order identity tensor. The  
49 main issue is the choice of  $L_c$ . For a shell structure problem, there are at least  
50 three different length scales candidates: the typical size of the whole structure  $L$ ,  
51 the element size  $h$  and the thickness  $t$ . Numerical experiments strongly suggest  
52  
53  
54  
55  
56  
57  
58  
59  
60  
61  
62  
63  
64  
65

1  
2  
3  
4  
5  
6  
7  
8  
9 that  $h \lesssim L_c < L$ . Indeed  $L_c \approx t$  usually gives an over-stiff discrete model  
10 and underestimated displacements, while the coercivity may be lost for  $L_c \approx L$ .  
11 190 Our experience has shown that, although  $L_c$  may be determined after a few  
12 trials,  $L_c \approx h$  is a safe default choice and is always satisfactory for moderate  
13 strains. However, this relation has to remain loose since the accuracy of the  
14 approximate gradient will deteriorate if  $L_c = h$  for very fine meshes (see [10])  
15 and the postprocessing benefit will then be lost. Therefore we understand  $L_c$   
16 195 as the typical mesh size of a coarse mesh able to capture the features of the  
17 solution. If the mesh is further refined to get a better accuracy,  $L_c$  is kept the  
18 same.  
19

20 However the stabilization tensor (14) usually fails when large strains occur.  
21 200 For instance, the cylindrical test cases presented in section 5.3 need a greater  
22 stabilization near the applied point forces, which means that the stabilization  
23 should adaptive, i.e. depending on the local state of strains/stresses, as already  
24 noted in [51, 52].  
25

26 The first attempt [15] to design an adaptive  $\tau$  was to make use of the material  
27 205 fourth order elasticity tensor  $\mathbf{C}$ , by defining

$$[\tau]_{IK} = \frac{1}{L_c} C_{IJKL} N_J N_L \quad \text{with} \quad [\mathbf{C}]_{IJKL} = \frac{\partial^2 \Psi}{\partial E_{IJ} \partial E_{KL}}. \quad (15)$$

28 However, this stabilization is also insufficient for large strains, notably when a  
29 Saint Venant-Kirchhoff model is considered since  $\mathbf{C}$  is then constant.  
30

31 Alternatively the viscous stabilization designed for the Navier-Stokes equa-  
32 tions [53] could be used, with  
33

$$[\tau]_{ik} = \frac{1}{L_c} \frac{\partial P_{iJ}}{\partial F_{kL}} N_J N_L. \quad (16)$$

34 210 Although this stabilization should intuitively grow with the local deformation  
35 gradient there is no control on the smallest eigenvalue of  $\tau$  and it may actually  
36 become very small, making the model unstable.  
37

38 All three of the above stabilizations fail at some point for the problems  
39 presented in section 5.3. See the Appendix C for the detailed results.  
40

41 215 Another DG stabilization strategy [51] is based on the observation that the

regions where the numerical instabilities develop usually coincide with the regions where the elasticity tensor becomes indefinite. A small amount of initial stabilization  $\tau_0$  is then increased with an adaptive term proportional to the lowest negative eigenvalue of the local elasticity tensor

$$\boldsymbol{\tau} = \frac{\beta}{L_c} \left( \tau_0 - \rho_{\min} \left( \frac{\partial \mathbf{P}_h}{\partial \mathbf{F}_h} \right) \right) \mathbf{I}, \quad (17)$$

where  $\beta$  is some scaling factor, and  $\rho_{\min}$  is the minimum negative eigenvalue of the tensor  $\frac{\partial \mathbf{P}_h}{\partial \mathbf{F}_h}$  locally evaluated, with  $\rho_{\min} = 0$  if the eigenvalues are all positive. This approach worked successfully for large strains experiments considered in [51]. However, our numerical experiments reported in Appendix C show only mitigated results for the shell problems considered in this paper, since the parameter  $\beta$  has to be tuned case by case.

Lately, a lower bound for the HMC stabilization has been derived in [18] for nonlinear elasticity

$$\boldsymbol{\tau} = \tau \mathbf{I} \quad \text{with} \quad \tau > \frac{C_o}{h_F} + \frac{C_\theta}{h_F}, \quad (18)$$

where  $h_F$  is the diameter of the face,  $C_o$  is a local constant depending only on the local mesh properties, and  $C_\theta$  is a local constant depending on both local and global eigenvalues of the elasticity tensor. The authors propose an astute way of solving the global eigenvalue problem by using an embedded Discontinuous Galerkin approximation. Moreover, although the optimal convergence of the gradient may be lost since this stabilization is of order  $1/h$ , it can be retrieved by using locally a polynomial degree  $k+1$  in the elements where the elasticity tensor is indefinite. However, this method being designed for simplexes, it cannot be included in our comparative study.

### 3.2. Proposed stabilization tensor

In this paper, we propose an empirical stabilization based on the maximum eigenvalue of the elasticity tensor, by choosing

$$\boldsymbol{\tau} = \frac{1}{2L_c} \rho_{\max} \left( \frac{\partial \mathbf{P}_h}{\partial \mathbf{F}_h} \right) \mathbf{I}, \quad (19)$$

with  $\rho_{\max}$  the maximum of the largest eigenvalue of the elasticity tensor evaluated at all the Gauss points of a given face. Therefore  $\tau$  is constant face by face and depends on the deformations gradient. This stabilization is related to the local Lax-Friedrichs numerical flux for the hyperbolic problems. Here are a few comments regarding equation (19).

- In the linear elasticity limit, the stabilization parameter becomes  $\tau = \frac{1}{2L_c}(2\mu + 3\lambda)\mathbf{I}$ . Moreover, when  $\nu = 0$ , it becomes equal to (14).
- For shell applications, we could notice that equation (19) adds a substantial stabilization near the point forces and the wrinkles, where the onset of instabilities usually occurs.
- In the nearly-incompressible limit of nonlinear hyperelastic models, our experience is that the stabilization has to be significantly increased for HDG to converge. Equation (19) provides such a mechanism since  $\rho_{\max}$  will grow as  $\nu \rightarrow 0.5$ .

All the results presented in this paper have been obtained using this stabilization mechanism, and selecting  $L_c$  along the guidelines mentioned above. For a detailed comparison of the performances of the above stabilizations, see Appendix C.

## 4. Implementation

### 4.1. Loading incrementation

Our load-control algorithm 1 is provided in Appendix A. It is based on the standard incrementation algorithm used in ABAQUS ([54]) with some minor modifications. Note that the external forces or prescribed tractions appearing in (13) are denoted with the generic term  $\mathbf{P}_{\max}$ . However,  $\mathbf{P}_{\max}$  is not directly prescribed, but an incremented fraction of it  $\mathbf{P} = \lambda\mathbf{P}_{\max}$  with the fraction coefficient  $0 \leq \lambda \leq 1$ .



The Newton-Raphson procedure is not allowed to do more than  $n_{\max}$  iterations. If the convergence is not obtained after  $n_{\max}$  iterations, the load increment is then decreased. On the contrary, if the convergence has been sufficiently fast for the last two increments, the increment magnitude is then increased. We take  $n_{\max} = 20$  and  $\lambda_{\text{init}} = 0.05$  as default values. This algorithm is found to work well for all the test cases we have studied in this article. Our algorithm also gives the final number of load increments  $n_{\text{inc}}$  and the total accumulated number of Newton-Raphson iterations  $n_{\text{tot}}$  in order to get an idea of the method's efficiency and stability.

#### 4.2. Newton-Raphson algorithm

At each step of the loading algorithm, the Newton-Raphson procedure is called to solve the nonlinear system (13). The procedure evaluates successive approximations  $(\mathbf{F}_h^l, \varphi_h^l, \hat{\varphi}_h^l)$  of the unknowns under the current load  $\mathbf{P}$  starting from the converged state at the previous load  $(\mathbf{F}_h^0, \varphi_h^0, \hat{\varphi}_h^0)$ . For each Newton step  $l$ , the system of equations (13) is linearized with respect to the Newton increments  $(\delta \mathbf{F}_h^l, \delta \varphi_h^l, \delta \hat{\varphi}_h^l) \in \mathbf{V}_h \times \mathbf{W}_h \times \mathbf{M}_h$ . These increments then satisfy the system

$$((\partial_{\mathbf{F}_h} \mathbf{P}_h) \delta \mathbf{F}_h^l, \nabla \mathbf{w})_{\mathcal{T}_h}$$

$$- \langle (\partial_{\mathbf{F}_h} \widehat{\mathbf{P}}_h \mathbf{N}) \delta \mathbf{F}_h^l + (\partial_{\varphi_h} \widehat{\mathbf{P}}_h \mathbf{N}) \delta \varphi_h^l + (\partial_{\hat{\varphi}_h} \widehat{\mathbf{P}}_h \mathbf{N}) \delta \hat{\varphi}_h^l, \mathbf{w} \rangle_{\partial \mathcal{T}_h} = r_1(\mathbf{w}), \quad (20a)$$

$$\langle (\partial_{\mathbf{F}_h} \mathbf{F}_h, \mathbf{G})_{\mathcal{T}_h} + (\delta \varphi_h^l, \nabla \cdot \mathbf{G})_{\mathcal{T}_h} - \langle \delta \hat{\varphi}_h^l, \mathbf{G} \mathbf{N} \rangle_{\partial \mathcal{T}_h} = r_2(\mathbf{G}), \quad (20b)$$

$$\langle (\partial_{\mathbf{F}_h} \mathbf{P}_h) \delta \mathbf{F}_h^l, \mathbf{Q} \rangle_{\mathcal{T}_h} - (\partial_{\mathbf{F}_h} (\partial_{\mathbf{F}_h} \Psi(\mathbf{F}_h))) \delta \mathbf{F}_h^l, \mathbf{Q} \rangle_{\mathcal{T}_h} = 0, \quad (20c)$$

$$\begin{aligned} & \langle (\partial_{\hat{\varphi}_h} \widehat{\mathbf{P}}_h \mathbf{N}) \delta \hat{\varphi}_h^l + (\partial_{\varphi_h} \widehat{\mathbf{P}}_h \mathbf{N}) \delta \varphi_h^l + (\partial_{\hat{\varphi}_h} \widehat{\mathbf{P}}_h \mathbf{N}) \delta \hat{\varphi}_h^l, \boldsymbol{\mu} \rangle_{\partial \mathcal{T}_h \setminus \Gamma_D} \\ & + \langle \boldsymbol{\tau} \delta \hat{\varphi}_h^l, \boldsymbol{\mu} \rangle_{\Gamma_D} = r_3(\boldsymbol{\mu}), \quad (20d) \end{aligned}$$

for all  $(\mathbf{G}, \mathbf{C}, \mathbf{w}, \boldsymbol{\mu}) \in \mathbf{V}_h \times \mathbf{V}_h \times \mathbf{W}_h \times \mathbf{M}_h$ , the right-hand side residuals are given by

$$r_1(\mathbf{w}) = \langle \mathbf{f}, \mathbf{w} \rangle_{\mathcal{T}_h} - (\mathbf{P}_h, \nabla \mathbf{w})_{\mathcal{T}_h} + \langle \widehat{\mathbf{P}}_h(\mathbf{F}_h^l, \varphi_h^l, \hat{\varphi}_h^l) \mathbf{N}, \mathbf{w} \rangle_{\partial \mathcal{T}_h}, \quad (21a)$$

$$r_2(\mathbf{G}) = -(\mathbf{F}_h, \mathbf{G})_{\mathcal{T}_h} - (\varphi_h^l, \nabla \cdot \mathbf{G})_{\mathcal{T}_h} + \langle \hat{\varphi}_h^l, \mathbf{G} \mathbf{N} \rangle_{\partial \mathcal{T}_h}, \quad (21b)$$

$$r_3(\boldsymbol{\mu}) = \langle \mathbf{t}, \boldsymbol{\mu} \rangle_{\Gamma_N} - \langle \widehat{\mathbf{P}}_h(\mathbf{F}_h^l, \varphi_h^l, \hat{\varphi}_h^l) \mathbf{N}, \boldsymbol{\mu} \rangle_{\partial \mathcal{T}_h \setminus \Gamma_D} - \langle \boldsymbol{\tau}(\hat{\varphi}_h^l - \varphi_D), \boldsymbol{\mu} \rangle_{\Gamma_D}. \quad (21c)$$

1  
2  
3  
4  
5  
6  
7  
8  
9 All the residuals (21) are evaluated at the current iterate  $(\mathbf{F}_h, \varphi_h^l, \hat{\varphi}_h^l)$ . The  
10 external forces  $\mathbf{f}$  and tractions  $\mathbf{t}$  are given by the current load  $\mathbf{P}$ . Note that  
11 equations (20a), (20b) and (20d) are the linearization of equations (13a), (13b)  
12 and (13d) respectively, while equation (20c) is the differentiation of (13c) with  
13 respect to  $\delta \mathbf{F}_h^l$  and yields the sensitivity of  $\mathbf{P}_h$  with respect to  $\mathbf{F}_h$ . In (20),  
14  
15 280  $(\partial_{\mathbf{F}_h} \cdot)$ ,  $(\partial_{\varphi_h} \cdot)$  and  $(\partial_{\hat{\varphi}_h} \cdot)$  denote the partial derivatives with respect to  $\mathbf{F}_h$ ,  $\varphi_h$   
16 and  $\hat{\varphi}_h$  respectively.  
17  
18  
19

20 After solving (20), the numerical approximations are then updated

$$21 \quad (\mathbf{F}_h^{l+1}, \varphi_h^{l+1}, \hat{\varphi}_h^{l+1}) := (\mathbf{F}_h^l, \varphi_h^l, \hat{\varphi}_h^l) + \alpha (\delta \mathbf{F}_h^l, \delta \varphi_h^l, \delta \hat{\varphi}_h^l), \quad (22)$$

22 where the coefficient  $\alpha$  is determined by a line-search algorithm in order to  
23  
24 285 optimally decrease the residual. This process is repeated and  $l$  is incremented  
25 until the residual norm is smaller than a given tolerance, typically  $10^{-7}$ .  
26  
27  
28  
29

### 30 4.3. Linear system resolution

31 At each step of the Newton-Raphson algorithm, the linearization (20) gives  
32 the following matrix system to be solved  
33

$$34 \quad \begin{pmatrix} \mathbb{A}^l & \mathbb{B}^l \\ \mathbb{C}^l & \mathbb{D}^l \end{pmatrix} \begin{pmatrix} \delta U^l \\ \delta \hat{U}^l \end{pmatrix} = \begin{pmatrix} R_{12}^l \\ R_3^l \end{pmatrix}, \quad (23)$$

35  
36 290 where  $\delta U^l$  and  $\delta \hat{U}^l$  are the vectors of degrees of freedom of  $(\delta \mathbf{F}_h^l, \delta \varphi_h^l)$  and  $\delta \hat{\varphi}_h^l$   
37 respectively. Following the HDG resolution strategy, the system (23) is first  
38 solved for the traces only  $\delta \hat{U}^l$   
39  
40  
41  
42  
43

$$44 \quad \mathbb{K}^l \delta \hat{U}^l = R^l, \quad (24)$$

45 where  $\mathbb{K}^l$  is the Schur complement of the block  $\mathbb{A}$  and  $R^l$  is the reduced residual  
46  
47

$$48 \quad \mathbb{K}^l = \mathbb{D}^l - \mathbb{C}^l (\mathbb{A}^l)^{-1} \mathbb{B}^l, \quad R^l = R_3^l - \mathbb{C}^l (\mathbb{A}^l)^{-1} R_{12}^l. \quad (25)$$

49  
50 291 The reduced system (24) involves fewer degrees of freedom than the full system  
51 (23). Moreover due to the discontinuous nature of the approximate solution  
52  $(\mathbf{F}_h, \varphi_h)$ , the matrix  $\mathbb{A}^l$  and its inverse are block diagonal, and can be computed  
53  
54  
55  
56  
57  
58  
59  
60  
61  
62  
63  
64  
65

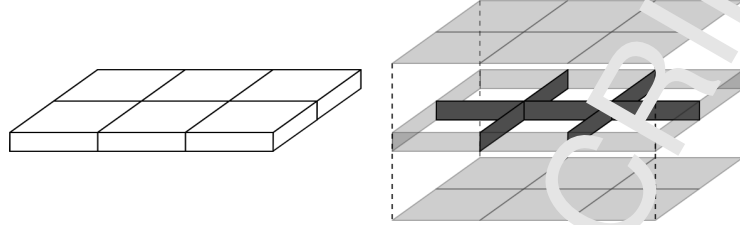


Figure 1: On the left is represented a simple thin rectangular structure. The support of the hybrid unknowns  $\delta\hat{\varphi}_h^l$  is on all the faces. On the right is represented, for the same structure, the support of the internal DoF  $\delta\hat{U}_I^l$  in dark gray and the support of the boundary DoF  $\delta\hat{U}_B^l$  in light gray. Only the internal DoF are actually globally coupled.

elementwise. Once  $\delta\hat{U}^l$  is known, the other unknowns  $U^l$  are then retrieved element-wise. Therefore, the full system (23) is never explicitly built, and the reduced matrix  $\mathbb{K}^l$  is build directly in an elementwise fashion, thus reducing the memory storage.

The global system (24) can be further reduced by eliminating the unknowns located on the boundary faces. If we denote the unknowns on the boundary faces by  $\delta\hat{U}_B^l$  and the unknowns on the interior faces  $\mathcal{E}_h^o$  by  $\delta\hat{U}_I^l$  such that  $\delta\hat{U}^l = (\delta\hat{U}_B^l, \delta\hat{U}_I^l)^T$ , the system (24) becomes

$$\begin{pmatrix} \mathbb{K}_{BB}^l & \mathbb{K}_{BI}^l \\ \mathbb{K}_{IB}^l & \mathbb{K}_{II}^l \end{pmatrix} \begin{pmatrix} \delta\hat{U}_B^l \\ \delta\hat{U}_I^l \end{pmatrix} = \begin{pmatrix} R_B^l \\ R_I^l \end{pmatrix}. \quad (26)$$

The geometric supports of  $\delta\hat{U}_B^l$  and  $\delta\hat{U}_I^l$  are illustrated in Fig 1. Thanks to the discontinuous nature of the approximation space  $\mathbf{M}_h$ , the matrix  $\mathbb{K}_{BB}^l$  is block diagonal and each block can be inverted independently. Therefore, we can efficiently reduce the system (26) to

$$\mathbb{K}_I^l \delta\hat{U}_I^l = R_R^l, \quad (27)$$

where

$$\mathbb{K}_I^l = \mathbb{K}_{II}^l - \mathbb{K}_{IB}^l (\mathbb{K}_{BB}^l)^{-1} \mathbb{K}_{BI}^l \quad \text{and} \quad R_R^l = R_I^l - \mathbb{K}_{IB}^l (\mathbb{K}_{BB}^l)^{-1} R_B^l. \quad (28)$$

For typical thin structures, the size of the global system (27) is about half of the original system (26). As a result, the global linear system (27) resulting

from the HDG method is cheaper to solve than those from other volumetric finite element methods. This makes the HDG method ideally suited for thin structures.

#### 4.4. Coupled degrees of freedom

Let us consider a simple thin structure such as a rectangular plate, as shown in in Fig. 1. This plate is divided into a regular 2D grid of  $N_x$  times  $N_y$  hexahedra elements (with only one element in the thickness direction). Such a structure contains a total of  $N_x(N_y + 1) + N_y(N_x + 1) + 2N_xN_y$  faces. Assuming that  $N_{\text{DOF}_{\text{face}}}$  degrees of freedom are associated to each face, there is a total of

$$N_{\text{DOF}_{\text{face}}} [N_x(N_y + 1) + N_y(N_x + 1) + 2N_xN_y] \quad (29)$$

degrees of freedom in the  $\delta\widehat{U}^l$  vector of the reduced system (24). Removing the degrees of freedom located on the boundary faces implies that  $2(N_xN_y + N_x + N_y)$  faces are excluded. That reduces the total number of degrees of freedom on the interior faces to be

$$N_{\text{DOF}_{\text{face}}} [N_x(N_y - 1) + N_y(N_x - 1)] \quad (30)$$

which is the size of the vector  $\delta\widehat{U}_I^l$  in the twice-reduced linear system (27). We see that, in this case, eliminating the boundary unknowns results in a reduction by half in the total number of coupled degrees of freedom.

#### 4.5. Arc-Length Algorithm

Our loading algorithm 1 is known to be unstable when snap-through behaviors appear. The Arc-Length algorithms ([55, 56]) address this shortcoming and are much more robust in the presence of complex snapping behaviors. We propose here an adaptation of the Arc-Length method to the HDG method.

The description of the Arc-Length method [2] is given in Appendix B. It makes uses of two user-defined parameters  $(\psi, \Delta l)$ . While the parameter  $\psi$  does not have much influence on the results, the characteristic length  $\Delta l$  controls the increment size, and has to be small enough to capture the snapping behavior. The classical Arc-Length method makes use of the global vector of nodal

displacement increments  $\delta\varphi_h$  in the process of determining both the load and  
 340 displacement increments. Interestingly, in the context of the HDG method, the  
 smaller vector of hybrid increments  $\delta\hat{\varphi}_h$  is used instead. The computation of  $\delta\lambda$   
 by solving a quadratic equations gives two possible increments and the choice  
 of the best increment is then based upon a comparison with the previously  
 converged increments (see e.g. [50]).

## 345 5. Numerical examples

In this section, we discuss the behavior of the present HDG solid element  
 formulation. We compare our numerical results with shell elements or analytical  
 solutions, when available. When a comparison with ABAQUS shell elements is  
 shown, it implies that a Saint Venant-Kirchhoff constitutive law has been used,  
 350 in order to be consistent with the ABAQUS-S4R element formulation [57]. We  
 use the loading algorithm 1 by default, and all results presented in this section  
 make use of the proposed stabilization (19).

Whenever a point force is applied, it is implemented as a nodal force. The  
 node is located on the external (resp. internal) surface for an outward (resp.  
 355 inward) force, in order to avoid the unpleasant  $\det(\mathbf{F}_h) \leq 0$  locally.

### 5.1. Numerical convergence test

In order to illustrate the convergence of the HDG method for thin structures,  
 we propose the following numerical test. A thin square plate of length  $L = 1$   
 and thickness  $t = 0.005$  is clamped on its four sides. A Saint Venant-Kirchhoff  
 360 model is considered with  $\mu = 1$  and  $\lambda = 2$ , i.e.  $\nu = 1/3$ . Body forces and traction  
 are prescribed to the plate such that the exact solution for the deformed  
 configuration is  $u_x = X, u_y = Y$ , and  $u_z = Z + 0.4 \sin(\pi X) \sin(\pi Y)$ , where  
 $\mathbf{X} = (X, Y, Z)^T$  are the coordinates of the undeformed plate. Fig. 2 shows the  
 undeformed plate, and the plate at maximum deformation.

We use the postprocessing presented in [11] to get a more accurate approxi-  
 mation of the deformation by making use of the approximate gradient. For each

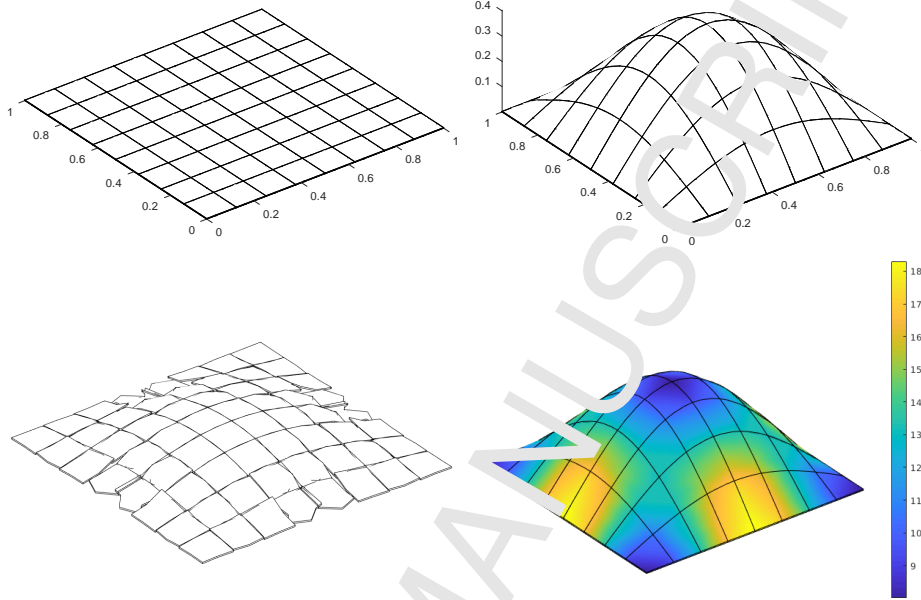


Figure 2: Top left: undeformed square plate. Top right : deformed square plate at maximum load. Bottom left : incipient instability for an insufficient penalization (14) at  $0.27 P_{\max}$ . Bottom right : distribution of  $\rho_{\max}$  at maximum load. Results are represented here for  $k = 2$  and a  $8 \times 8$  mesh.

$K \in \mathcal{T}_h$ , we build the post processed variable  $\varphi_h^* \in \mathcal{P}_{k+1}(K)^d$  such as

$$(\nabla_{\mathbf{r}_h}^* \nabla \mathbf{w})_{\mathcal{T}_h} = (\mathbf{F}_h, \nabla \mathbf{w})_{\mathcal{T}_h}, \quad \forall \mathbf{w} \in \mathcal{P}_{k+1}(K)^d \quad (31a)$$

$$(\varphi_h^*, 1)_{\mathcal{T}_h} = (\varphi_h, 1)_{\mathcal{T}_h}. \quad (31b)$$

365 The table 1 shows the errors of the HDG results and the estimated orders of convergence (e.o.c.) when the mesh is refined uniformly in the  $e_x$  and  $e_y$  directions. All simulations make use of only one element in the thickness direction. Polynomial orders  $k \in \{1, 2, 3\}$  are considered, and the adaptive stabilization is given by (19) with  $L_c = 0.5$  as characteristic length.

370 The optimal order of convergence  $k + 1$  is observed for the displacement at all polynomial degrees. The observed order of convergence of the gradient varies between  $k + \frac{1}{2}$  and  $k + 1$ . Accordingly, the postprocessed displacement converges with orders between  $k + \frac{3}{2}$  and  $k + 2$ . Note that, by varying the values

of  $t$  and  $\nu$ , slightly different orders of convergence may be observed, but the  
 375 previous observations remain valid. See, for instance, the s.o.c in the nearly-  
 incompressible limit (with  $\mu = 1$  and  $\nu = 0.49999$ ) reported in table 2. Also,  
 in order to get an accurate postprocessing,  $L_c$  has to be large enough, typically  
 $L > L_c \gg t$ .

Interestingly, for a linear elastic body and for the mesh sizes considered,  
 380 the optimal orders of convergence are achieved for a small uniform  $\tau_{ii} \leq 0.5$ .  
 However, that level of stabilization would be clearly insufficient in the nonlinear  
 case and the Newton algorithm would quickly diverge. Even the higher amount  
 of uniform stabilization given by (14) would fail at some point before  $\mathbf{P}_{\max}$   
 is reached. On the contrary, our adaptive stabilization is successful by using  
 385 higher values  $8 \leq \tau_{ii} \leq 19$ , and the areas where the stabilization is large seems  
 to match the areas of incipient instabilities (see Fig. 2, bottom). Therefore, we  
 believe that the discrepancy between the amount of stabilization expected to  
 converge optimally, and the one needed to stabilize the nonlinear model at finite  
 strains is the cause of the slightly suboptimal orders of convergence observed  
 390 for the gradient.

Although the postprocessing may not always achieve an extra full order of  
 convergence, it always computes a significantly more accurate displacement, at  
 a negligible cost. It therefore remains an attractive feature of the HDG approach.  
 Consequently, all the results presented in this paper are the postprocessed dis-  
 395 placements.

## 5.2. Cantilever problems

### 5.2.1 Cantilever subjected to a lifting force

Let us consider a cantilever of length  $L = 10$  m, width  $l = 1$  m and thickness  
 $= 0.1$  m, with mechanical properties  $E = 1.2 \times 10^6$  kPa and  $\nu = 0$ . The  
 400 cantilever is clamped at one end, and is subjected to a lifting force  $\mathbf{P} = 4$  kPa at  
 the other end (see Fig. 3). The lifting force is usually a distributed line force when  
 shell elements are considered (for instance [58, 59, 60]). Here the corresponding  
 force is applied through a Neumann boundary condition prescribing the traction

$k$	mesh size $h$	$\ \varphi - \varphi_h\ $	e.o.c	$\ \mathbf{F} - \mathbf{F}_h\ $	e.o.c	$\ \varphi - \varphi_h^*\ $	e.o.c
1	0.5000	2.08e-03	-	2.15e-02	-	2.38e-03	-
	0.2500	8.54e-04	1.28	7.06e-03	1.61	2.88e-04	3.05
	0.1667	3.99e-04	1.88	3.80e-03	1.53	1.01e-04	2.58
	0.1250	2.34e-04	1.86	2.44e-03	1.54	4.80e-05	2.60
	0.0833	1.08e-04	1.92	1.31e-03	1.54	1.66e-05	2.62
	0.0625	6.15e-05	1.94	8.11e-04	1.53	7.77e-06	2.63
2	0.5000	3.04e-04	-	2.14e-03	-	1.16e-04	-
	0.2500	3.19e-05	3.25	2.66e-04	3.01	8.32e-06	3.80
	0.1667	1.01e-05	2.85	8.79e-05	2.73	1.77e-06	3.81
	0.1250	4.34e-06	2.92	3.80e-05	2.91	5.69e-07	3.95
	0.0833	1.36e-06	2.97	1.17e-05	2.91	1.16e-07	3.93
	0.0625	5.52e-07	2.98	5.13e-06	2.87	3.77e-08	3.90
3	0.5000	2.61e-05	-	4.69e-04	-	2.15e-05	-
	0.2500	2.70e-06	3.30	2.19e-05	4.42	4.26e-07	5.66
	0.1667	5.52e-07	4.01	5.44e-06	3.43	6.34e-08	4.70
	0.1250	1.74e-07	3.89	1.90e-06	3.66	1.76e-08	4.45
	0.0833	3.53e-08	3.94	4.24e-07	3.69	2.95e-09	4.41
	0.0625	1.13e-08	3.96	1.48e-07	3.64	7.86e-10	4.60

Table 1: History of convergence of the HDG method for the sinusoidally loaded plate, and for a compressible material ( $\nu = 1/3$ ).



$k$	mesh size $h$	$\ \varphi - \varphi_h\ $	e.o.c	$\ \mathbf{F} - \mathbf{F}_h\ $	e.o.c	$\ \varphi - \varphi_h^*\ $	e.o.c
1	0.5000	2.22e-03	-	2.37e-02	-	2.43e-03	-
	0.2500	6.75e-04	1.72	7.86e-03	1.59	3.06e-04	2.99
	0.1667	3.18e-04	1.85	4.25e-03	1.51	1.20e-04	2.30
	0.1250	1.87e-04	1.84	2.72e-03	1.56	6.07e-05	2.38
	0.0833	8.66e-05	1.90	1.54e-03	1.56	2.26e-05	2.43
	0.0625	4.96e-05	1.94	9.22e-04	1.56	1.10e-05	2.48
2	0.5000	2.72e-04	-	1.40e-03	-	1.14e-04	-
	0.2500	2.61e-05	3.38	3.64e-04	2.72	1.35e-05	3.42
	0.1667	7.81e-06	2.98	1.19e-04	2.75	2.84e-06	3.84
	0.1250	3.26e-06	3.04	5.20e-05	2.89	9.00e-07	3.99
	0.0833	9.57e-07	3.04	1.59e-05	2.91	1.78e-07	3.99
	0.0625	3.97e-07	3.03	6.88e-06	2.92	5.70e-08	3.97
3	0.5000	1.76e-05	-	7.08e-04	-	3.64e-05	-
	0.2500	4.47e-06	3.42	3.08e-05	4.52	6.40e-07	5.83
	0.1667	8.87e-07	3.99	5.71e-06	4.15	6.24e-08	5.74
	0.1250	2.88e-07	3.90	2.07e-06	3.53	1.59e-08	4.74
	0.0833	5.81e-08	3.95	5.06e-07	3.47	2.67e-09	4.40
	0.0625	1.85e-08	3.97	1.84e-07	3.50	7.63e-10	4.36

Table 2: History of convergence of the HDG method for the sinusoidally loaded plate, and for a nearly-incompressible material ( $\nu = 0.49999$ ).

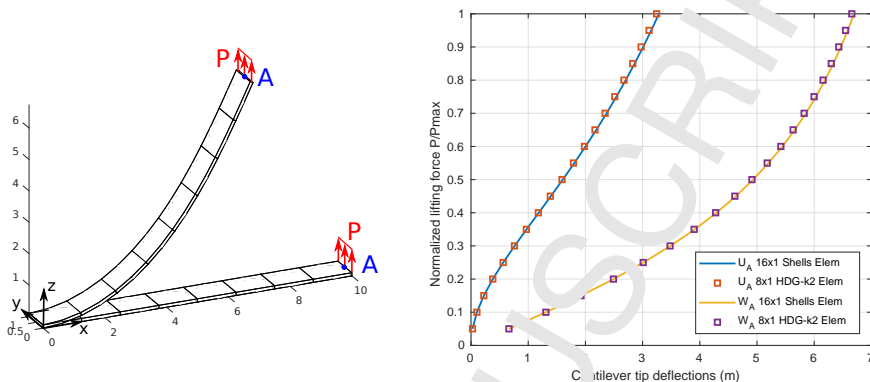


Figure 3: Cantilever subjected to a lifting force. Left: cantilever undeformed, and under the maximum deformation, for a  $8 \times 1$  mesh and with the lifting force  $P$ ; corresponding deflections of the cantilever's tip, recorded at point A. Results from  $8 \times 1$  S4R shell elements are reported as a reference.

$\mathbf{t} = \mathcal{A}^{-1}\mathbf{P}$  with  $\mathcal{A}$  the cantilever endoreciprocity. The adaptive stabilization (19) is used with  $L_c = 1$  m. The displacements of the lifted tip are reported on Fig. 3 and show a good agreement when compared to S4R shell elements when quadratic HDG elements ( $k = 2$ ) are used. For linear HDG elements, at least 50 elements would have been necessary to get reasonably accurate results.

### 5.2.2. Cantilever subjected to a bending moment

The following example is a very popular benchmark considered by [59, 60] and others. The purpose of this benchmark is to test the modeling of large bending deformations for thin beams. We consider the same cantilever as before, but slightly longer ( $L = 12$  m). Instead of a lifting force, the cantilever is now subject to a maximum bending moment  $M_{\max} = \frac{50\pi}{3} \times 1000 \text{ kN m}^{-1}$  at its other end (see Fig. 4, left). The bending moment is numerically applied as a Neumann boundary condition, prescribing on the tip surface an equivalent normal traction  $\mathbf{t}$  varying linearly in the vertical direction. For an applied moment  $0 \leq M \leq M_{\max}$ , analytical solutions give the horizontal and vertical displacements of a tip point A located on the mean surface

$$U_A = L \frac{M_{\max}}{2\pi M} \sin\left(\frac{2\pi M}{M_{\max}}\right) + L \quad \text{and} \quad W_A = L \frac{M_{\max}}{2\pi M} \left(1 - \cos\left(\frac{2\pi M}{M_{\max}}\right)\right).$$

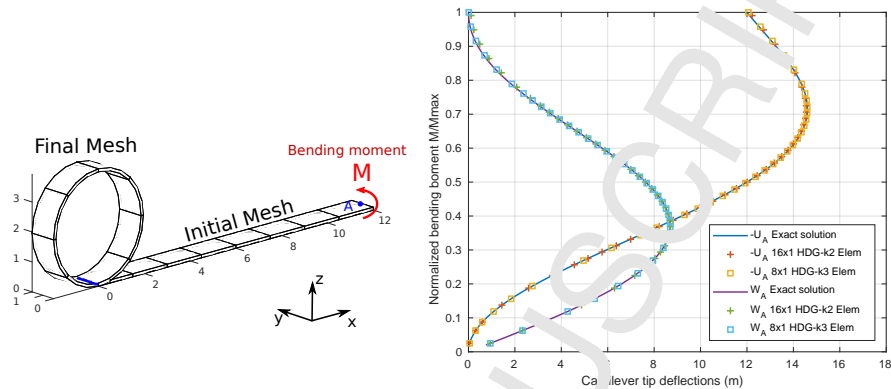


Figure 4: Cantilever subjected to a bending moment. Left : cantilever undeformed, and under the maximum deformation, for a  $8 \times 1$  mesh and with  $k = 3$ . Right : corresponding deflections of the cantilever's tip, recorded at point 12. The exact solution is also shown, as well as a solution performed with a  $16 \times 1$  mesh and  $k = 2$ .

410 The displacements of the tip are reported on Fig. 4, right, for both quadratic and cubic HDG elements, and the adaptive stabilization is the same as before. Converged results are obtained with a  $16 \times 1$  mesh for quadratic elements and a  $8 \times 1$  mesh for cubic elements.

### 5.3. Shell problems

#### 415 5.3.1. Slit annular plate

The slit annular plate benchmark checks the accuracy of the combined bending and torsional deformations. Let us consider a slit annular plate of internal radius  $r = 6$  m, external radius  $R = 10$  m and thickness  $t = 0.03$  m clamped at one end of the slit and subjected to a lifting force  $\mathbf{P}$  at the other end (see Fig. 5, 420 left). The force with a maximum magnitude 0.8 kN is applied as a traction distributed over the slit end. The material parameters are  $E = 21 \times 10^6$  kPa and  $\nu = 0$ . We use  $L_c = 1$  m, for the adaptive stabilization. For  $k = 2$ , the converged HDG results on a  $6 \times 30$  mesh are in excellent agreement with the reference results computed with S4R shell elements (see Fig. 5, right).

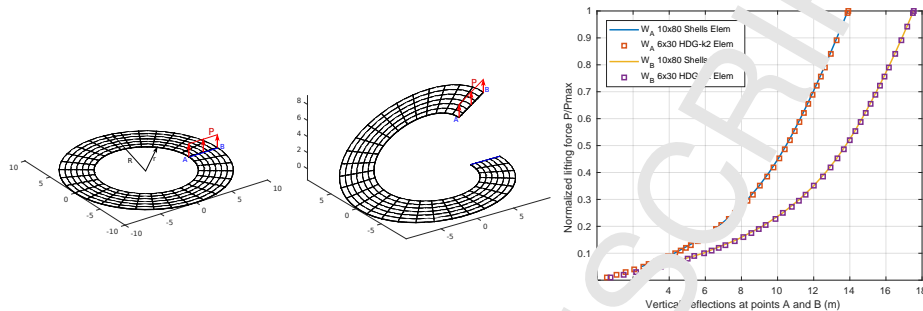


Figure 5: Slit annular plate subjected to a lifting force. Left : plate undeformed, and under the maximum deformation, for a  $6 \times 30$  mesh and with  $k = 2$ . Right : corresponding deflections of the lifted end, recorded at points A and B. A reference solution computed with a mesh of  $10 \times 80$  S4R shell elements is also displayed.

### 5.3.2. Hemispherical shell with a $18^\circ$ hole

We present here the hemispherical shell problem considered by [61, 59, 27, 60, 26, 30] and others. This benchmark tests the ability to model combined large membrane and bending deformations in double-curved shell geometries.

The structure studied is a hemispherical shell with a  $18^\circ$  centered circular hole. The material properties considered are  $E = 6.825 \times 10^7$  kPa,  $\nu = 0.3$ . The radius of the hemisphere is  $R = 10$  m and its thickness is  $t = 0.04$  m. The shell is subjected to two alternating radial point forces, whose magnitude are  $P = 400$  kN each (see Fig. 6, left). Due to the symmetries, the computational domain is only one quarter of the full problem. Symmetry boundary conditions are then applied (see Fig. 6, right).

The HDG solution for the deflections at the nodes A and B is computed with an  $8 \times 8$  mesh, using polynomial order  $k = 3$  and the adaptive  $\tau$  is computed with  $\omega_c = 3$  m. For  $k = 2$ , converged results are obtained for a finer mesh of  $20 \times 20$  elements. The results, given in Fig. 7 show an excellent agreement with the reference solution presented in [60] which is computed with  $16 \times 16$  S4R shell elements.

In order to illustrate how the right amount of stabilization mitigates the locking pathologies, we also display the displacements obtained by using a very large  $\tau_m = 1000\mu$  instead of the adaptive  $\tau$ , for the same quadratic mesh.

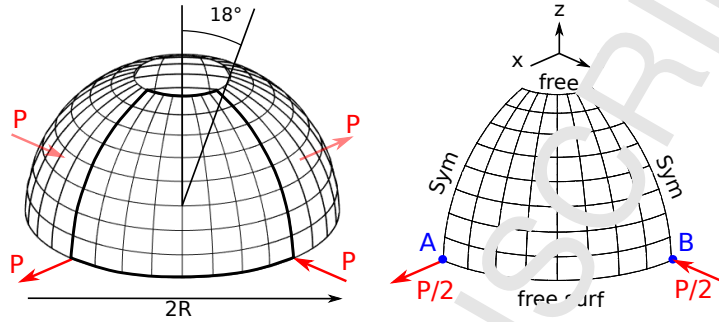


Figure 6: Left : cylindrical shell dimensions and applied point forces. Right : reduced computational domain and boundary conditions. Here a  $2 \times 8$  mesh is used, with  $k = 3$ .

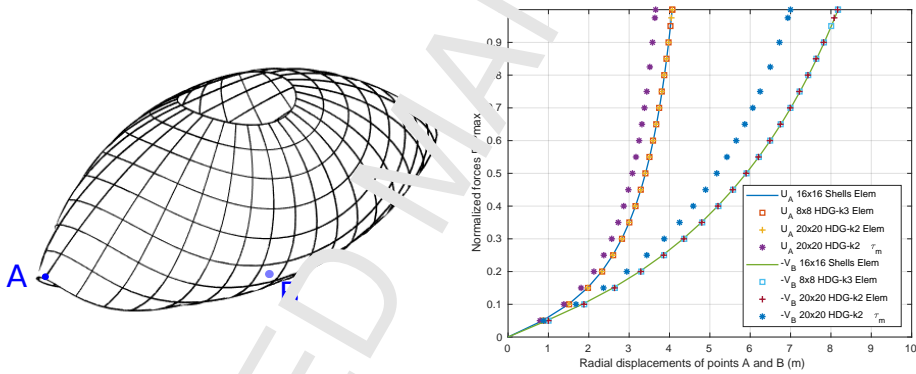


Figure 7: Left : deformed hemispherical shell under maximum load. Right : radial deflections of points  $A$  and  $B$  are compared against a shell elements reference result.

445 Clearly the deflections become severely underestimated and the HDG model  
 446 *locks*. As continuous Galerkin can be regarded as a limit of HDG [48] when  
 447  $\tau \rightarrow \infty$  we expect that similar deflections would be obtained with a standard  
 448 continuous Galerkin method.

### 5.3.3. Pullout of an open-end cylinder

450 The pullout of a cylindrical shell with free edges is a benchmark used to  
 451 check the accuracy in modeling large bending and membrane deformations. We  
 452 consider a cylinder of radius  $R = 4.953$  m, length  $L = 10.35$  m and thickness  
 453  $t = 0.094$  m, subjected to a pair of symmetrical radial pulling forces  $\mathbf{P}$  whose

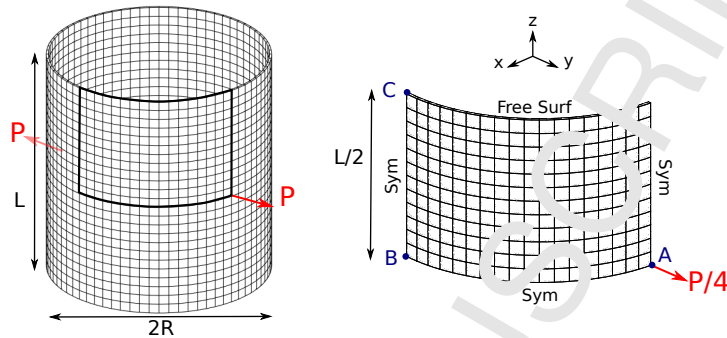


Figure 8: Left : cylinder dimensions and applied point force. Right : reduced computational domain and boundary conditions. Here a  $12 \times 18$  mesh is represented, and  $k = 2$ .

maximal magnitudes are  $P_{\max} = 4 \times 10^4 \text{ N}$ . Material properties are  $E =$   
 455  $10.5 \times 10^6 \text{ kPa}$  and  $\nu = 0.3125$ . Owing to symmetries, only one eighth of the  
 structure is modeled, using the suitable symmetric boundary conditions (see  
 Fig. 8). Based on the mesh size, the characteristic length is  $L_c = 0.4 \text{ m}$ .

Accurate results are obtained with a  $12 \times 18$  mesh for quadratic ( $k = 2$ )  
 elements (see Fig. 8 and 9). For  $k = 3$ , a similar accuracy is obtained with a  
 460  $8 \times 12$  mesh. Note that, although refining the mesh does not lead to a significant  
 modification ( $< 1\%$ ) of the deflection of points  $B$  and  $C$ , it will slightly increase  
 the deflection of point  $A$ , where the force is applied. This is due to a local 3D  
 effect, which is amplified when the support of the point force shrinks.

The displacements of all three points  $A$ ,  $B$  and  $C$ , match very well the  
 465 reference solution computed with  $24 \times 36$  S4R shell elements (see Fig. 9).

The table C.6 gives the solver metrics as well as a comparison between  
 different stabilizations. Interestingly, by using the same characteristic length  $L_c$ ,  
 most stabilization functions would fail to reach  $P_{\max}$ . By using (19), a sufficient  
 amount of stabilization is provided near the point force, and the number of load  
 470 increments is  $n_{\text{inc}} = 26$ . However, Fig. 9, right, displays more data points for  
 the sake of comparison by using artificially lower load increments.

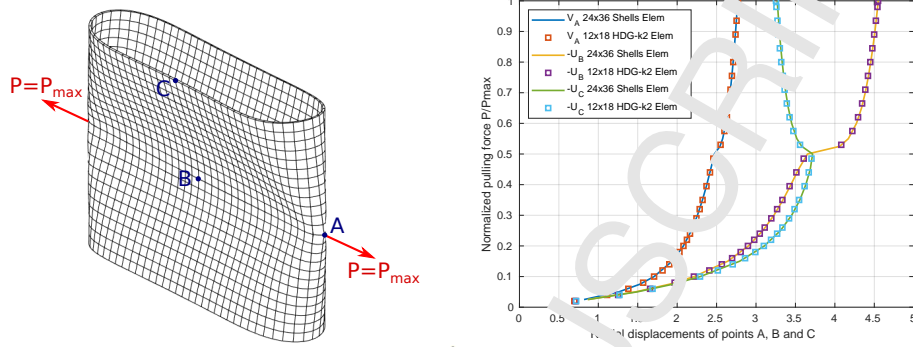


Figure 9: Left : deformed cylindrical shell under maximum load, for a  $12 \times 18$  quadratic elements mesh. Right : radial deflections at points  $A$ ,  $B$  and  $C$  are compared against a shell elements reference result.

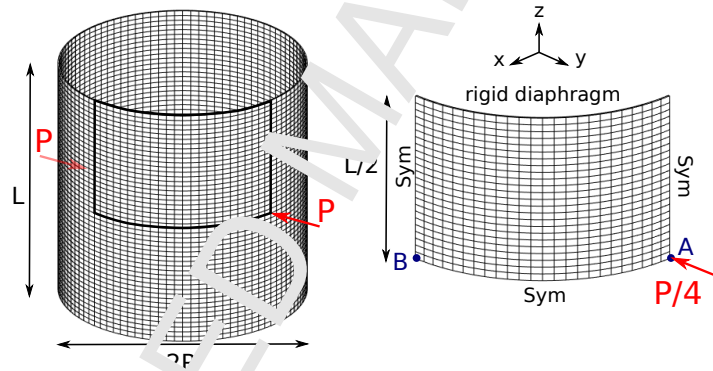


Figure 10: Left : cylindrical shell dimensions and applied point forces. Right : reduced computational domain and boundary conditions. Here a  $48 \times 48$  mesh is used, and  $k = 2$ .

#### 5.3.4. *Pinned cylinder with end diaphragms*

The pinned cylindrical shell is one of the most demanding classical benchmark that can be found in the literature. Simo et al [62] explained that the difficulty comes from the inextensional bending and the complex membrane states of stress. The deformations involve the development of wrinkles, which are quite hard to model with low order elements or with coarse meshes, and most of the finite elements formulations have a hard time converging for this particular example (see for instance [28]).

We consider a cylinder represented on Fig. 10, whose radius is  $R = 10$  m,

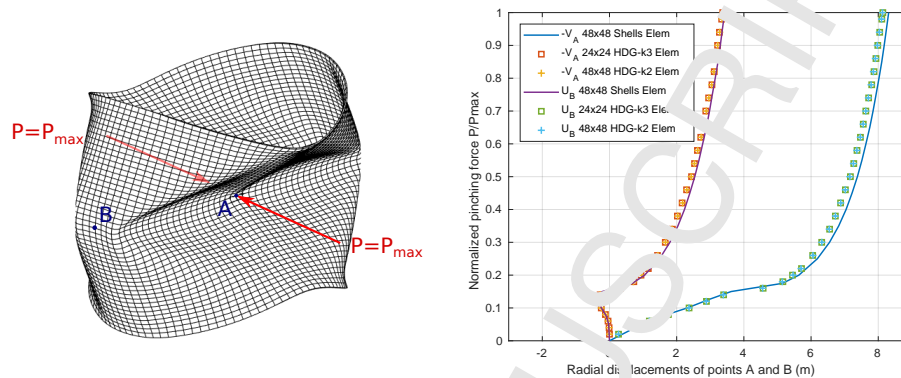


Figure 11: Left : deformed cylindrical shell under maximum load, for a  $24 \times 24$  cubic elements mesh. Right : corresponding radial deflections at points  $A$  and  $B$  being compared against a  $48 \times 48$  S4R shell elements reference result (only selected data points are displayed).

length  $L = 20$  m and thickness  $t = 0.1$  m. The cylinder is subjected to a pair of symmetrical radial pinching forces  $\mathbf{P}$  whose maximal magnitudes are  $P_{max} = 120$  kN. The cylinder is closed with rigid diaphragms on its ends such that the ends points can only move in the  $z$ -direction. Thanks to the different symmetries in the problem, only one octant of the geometry needs to be modeled (see Fig. 10). Converged results are obtained when the octant is meshed with a  $48 \times 48$  mesh for polynomial order  $k = 2$ . Alternatively, for  $k = 3$ , the results converge for a coarser  $24 \times 24$  mesh. We picked  $L_c = 0.25$  m for the stabilization. Without the proper adaptive mechanism, most stabilizations fail for that case or induce a non-physical oscillatory behavior (see table C.7).

The computed radial deflections at points  $A$  and  $B$  show a globally good agreement with the S4R solution, although HDG predicts slightly smaller deflections for the point  $A$  at large deformations. Such level of discrepancies between numerical methods are however common for the pinched cylinder case (see [63, 64]). For this specific case, the Newton-Raphson procedure converges rather slowly and we increased the maximum number of Newton iterations to 50. For  $k = 2$ , the total number of load increments and Newton iterations are  $n_{inc} = 50$  and  $n_{tot} = 468$  respectively, which is comparable to the the S4R results (respectively 70 and 406, according to [60]).



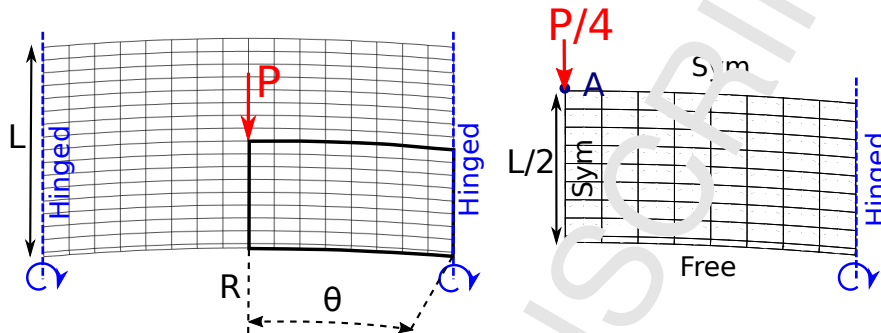


Figure 12: Left : full roof structure with boundary conditions. Right : quarter of the full structure actually modeled.

### 500 5.3.5. Hinged roof

The following numerical experiment was introduced first in [65] and since then has been extensively studied as an example of snapping instabilities.

The roof structure is a section of a cylindrical shell hinged on two sides, with radius  $R = 25.4$  m, length  $L = 2.54$  m, and angle  $\theta = 0.1$  rad (see Fig. 12). A vertical point load  $P_{\max} = 300$  N is applied at the center of the structure. The material properties are  $E = 3102.75$  kPa and  $\nu = 0.3$ . Only one quarter of the full structure is modeled and converged results are obtained using an  $8 \times 8$  quadratic element mesh. The characteristic length is therefore  $L_c = 0.3$  m.

As a side note, in order to implement the *hinged* boundary conditions we found it more practical to strongly enforce all the Dirichlet-like boundary conditions (including the hinged ones). Therefore, for this specific numerical experiment, the variational principle (5), the HDG trace equation (13d) and the space of traces (3) should all be modified accordingly.

The behavior of the structure changes dramatically with the thickness of the roof. For a thick roof, i.e.  $t = 127$  mm, the structure exhibits a snap-through instability, whereas for a thinner roof, i.e.  $t = 63.5$  mm, a snap-back instability is observed (see Fig. 13).

The Newton-Raphson algorithm typically fails on either configuration, because the Jacobian matrix in (23) becomes singular for loads smaller than  $P_{\max}$ .

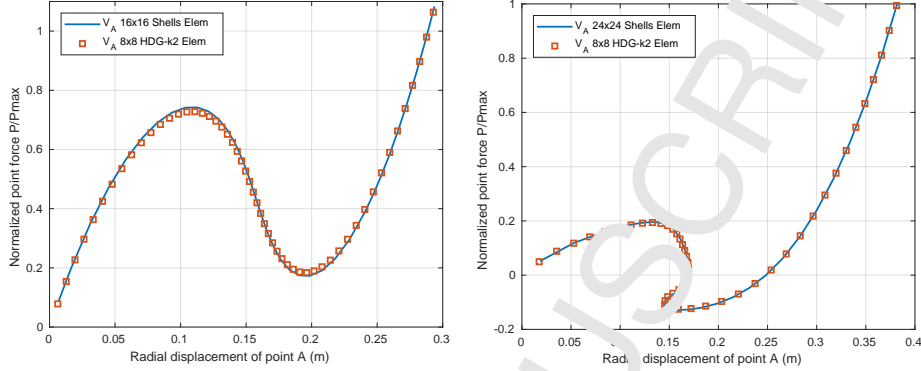


Figure 13: Results obtained for a  $8 \times 8$  mesh with  $\nu = 2$ . Left : radial deflection of point  $A$  for  $t = 127$  mm, and comparison against a  $16 \times 16$  S4R shell element result. The snap-through instability arises at 72.5% of the maximum load. Right : radial deflection of point  $A$  for  $t = 63.5$  mm compared against a  $24 \times 24$  shell elements result. The first snap-through instability arises around 20% of the total load, while the first snap-back instability appears around 1%.

520 We therefore use the Arc-Length algorithm 2 with parameters

$$\psi = \frac{1}{0.1 \|\mathbf{P}_{\max}\|} \quad \text{and} \quad \Delta l = \begin{cases} 0.2 \text{ m} & \text{if } t = 127 \text{ mm} \\ 0.3 \text{ m} & \text{if } t = 63.5 \text{ mm} \end{cases} \quad (32)$$

525 The converged deflection at the center of the roof, shown on Fig. 13, essentially agree with the results obtained using ABAQUS standard S4R shell elements. The full snapping behaviors are properly modeled, and the instabilities are handled correctly by the Arc-Length method. Although the agreement is excellent for the thin roof, the snap-through occurs slightly earlier with HDG for the thick roof (72.5% of the total load instead of 74% for the shell elements).

#### 5.4. Thick-thin structure

57 We now present an simple example of a thick solid-thin shell structure. The structure is composed of a thick pillar supporting an arch with a variable thickness (see Fig. 14). The thickness of the arch is 0.5 m at the root, and 0.025 m at the tip. The 2D geometry presented on Fig. 14 is extruded 0.5 m in the normal direction. The base of the pillar is clamped and an uniform pressure  $\mathbf{P}$

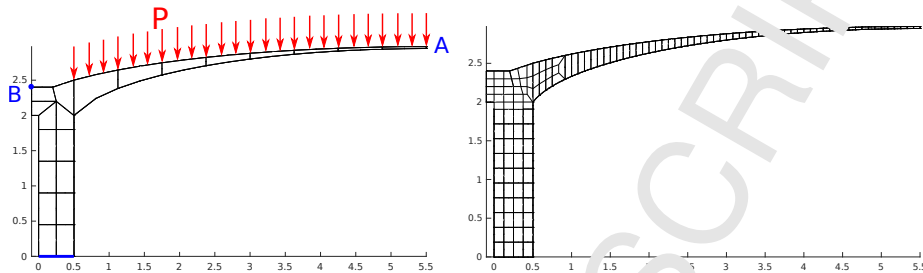


Figure 14: Meshes used for the thick-thin arch structure. Left: coarse mesh modeling the arch with 8 elements, with  $k = 2$ . The pressure is applied on the arch on  $\Gamma$ . Right: fine mesh modeling the arch with 68 elements, and with  $k = 3$ . Reference results are computed using the fine mesh.

	$U_A$	$V_A$
Coarse Mesh	-0.1411	-0.9796
Reference Mesh	-0.1405	-0.9453

Table 3: Horizontal and vertical deflections of the point A obtained with a coarse mesh and a fine reference mesh.

is applied on the upper side of the arch such that the total integrated pressure is equivalent to a 100 kN force. A neo-Hookean model with  $E = 200$  GPa and  $\nu = 0.28$  is used.

Two discretizations are considered. The first one uses a coarse mesh with  $k = 2$ , modeling the arch with only 8 elements. Therefore the element aspect ratios vary from almost 1 (near the pillar) to 20 (near the tip). A second discretization, used to generate the reference solution, makes use of a finer mesh with  $k = 3$ . By using 68 elements for modeling the arch, the aspect ratio is kept small for all the elements. For both meshes, the final deflections of the arch tip (point A) are recorded. For both numerical simulations, we will take  $L_c = 1$  m.

The results under maximum load are reported on table 3. The coarse mesh exhibit a good accuracy for the deflection of point A although the vertical displacement is slightly overestimated. This example confirms that our approach, making use of volumetric elements, is indeed suitable for thin-thick structures.

### 5.5. Realistic structure: wing mesh

While all the applications presented so far can be easily run on a single CPU core, many complex realistic structures will need more computational resources. We have therefore implemented a parallel version of our method that make use of the HDG solver previously developed for CFD applications (see [66]). The global system (27) is solved by a parallel Generalized Minimal Residual (GMRES) method, using a block incomplete LU (BILU) factorization as a left preconditioner.

We have used this parallel solver to compute the deformations of a complex aircraft wing structure, comprising an upper and a lower skin, spars and multiple ribs (see [67] for a precise description of the geometry). The mesh consists of 13382 hexahedra whose aspect ratio varies between 1.1 and 75. Although the parallel solver can solve nonlinear problems, we consider here a linear application in order to provide some indication of the code efficiency in solving a single linearized step. The linear elastic moduli are  $E = 70$  GPa and  $\nu = 0.35$  for the whole structure. The wing root is clamped, and a traction equivalent to a 200 kN lifting force is applied on the wing tip. A polynomial degree  $k = 2$  is considered, and the characteristic length is set to  $L_c = 0.1$  m. Fig. 15 shows the deformed wing as well as the distribution of the Von Mises stresses.

The parallel code ran on 2 Haswell nodes of the NASA Pleiades supercomputer, each node being a 12-cores Intel Xeon E5-2680v3 at 2.50 GHz. The resolution of the linear system lasted approximately 10 min, with GMRES needing around 1000 iterations to converge. The BILU preconditioner, which is more suited for hyperbolic problems, is probably the cause of the relatively high number of iterations. We believe that a specific preconditioner for elastostatic HDG applications should therefore be developed.

## 6. Conclusion

We have presented a HDG method for solving nonlinear elastic structures including thin components. Our approach models the full 3D structure and does

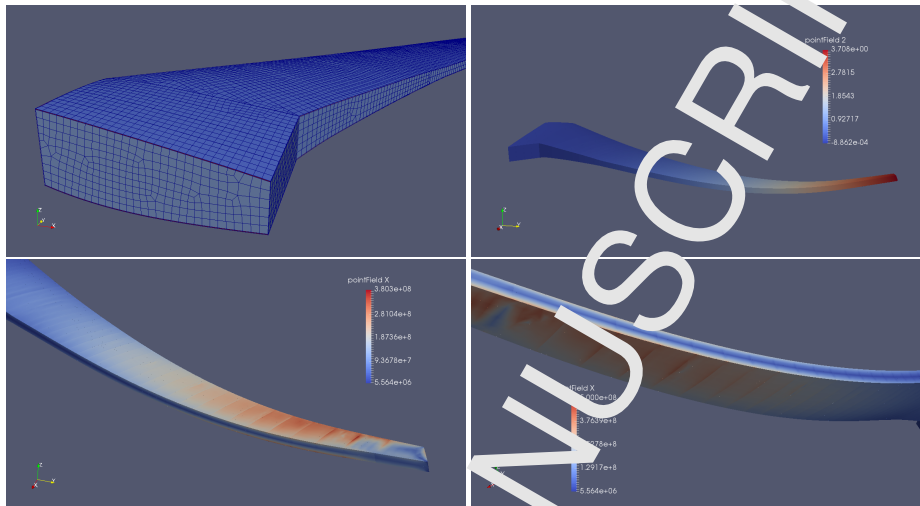


Figure 15: Static analysis of an airliner wing structure. Top left: mesh of the wing – zoom on the wing root. Top right: vertical displacements at maximum load. Bottom: Von Mises stress distribution on the upper skin (left) and on the lower skin (right). The concentration of stresses at the connection between the ribs and the skin is clearly visible, showing the strengthening effect of the ribs.

not require typical approximations used in shell theories. The size of the global systems of equations can be significantly reduced when thin structures are modeled, which is an appealing feature compared to other volumetric approaches. Moreover, optimal rate of convergence for the deformation is observed, and the postprocessing provides between one half and one full extra order of convergence at a negligible cost. We have validated our method studying classical benchmarks for both cantilever and shell structures. Our numerical results show that when quadratic or cubic polynomial approximations are used, the method is free from locking and gives accurate converged results. The HDG approach is therefore worth considering for modeling finite deformations of shell structures.

### Acknowledgments

The authors gratefully acknowledge the NASA for supporting this work under grant number NNX16AP15A. The authors particularly thanks Steven J.

1  
2  
3  
4  
5  
6  
7  
8  
9 Massey for providing the wing mesh and an access to the NAS computational  
10 resources.  
11

12 The first author warmly thanks Pablo Fernandez del Campo for his help  
13 regarding the development and the use of the parallel version of the code.  
14

15  
16 **Appendix A. Loading algorithm**  
17  
18  
19  
20  
21  
22  
23  
24  
25  
26  
27  
28  
29  
30  
31  
32  
33  
34  
35  
36  
37  
38  
39  
40  
41  
42  
43  
44  
45  
46  
47  
48  
49  
50  
51  
52  
53  
54  
55  
56  
57  
58  
59  
60  
61  
62  
63  
64  
65

**Algorithm 1** Load incrementation algorithm

**Require:** Initialize  $\mathbf{F}_h^0 = \mathbf{Id}$  ;  $(\boldsymbol{\varphi}_h^0, \hat{\boldsymbol{\varphi}}_h^0) = \mathbf{X}$  (initial geometry)

**Require:** Initialize  $\lambda = \lambda_{\text{init}}$  ;  $\mathbf{P} = \lambda \mathbf{P}_{\text{max}}$  ;  $n_{\text{tot}} = 0$  ;  $n_{\text{inc}} = 0$  ;  $n_{\text{it1}} = 0$

**while**  $\lambda < 1$  **do**

    Assign  $\lambda := \lambda + \Delta\lambda$

    Assign  $\mathbf{P} := \lambda \mathbf{P}_{\text{max}}$

*Call of the Newton-Raphson procedure, converging in  $n_{\text{it}}$  iterations*

    Compute  $(\mathbf{F}_h, \boldsymbol{\varphi}_h, \hat{\boldsymbol{\varphi}}_h, n_{\text{it}}) = \text{Newton-Raphson}(\mathbf{F}_h^0, \boldsymbol{\varphi}_h^0, \hat{\boldsymbol{\varphi}}_h^0, \mathbf{P})$

**if**  $n_{\text{it}} \leq n_{\text{max}}$  **then**

*Convergence of Newton-Raphson.*

        Assign  $(\mathbf{F}_h, \boldsymbol{\varphi}_h, \hat{\boldsymbol{\varphi}}_h) := (\mathbf{F}_h^0, \boldsymbol{\varphi}_h^0, \hat{\boldsymbol{\varphi}}_h^0)$

**if**  $n_{\text{it}} < 5$  **and**  $n_{\text{it1}} < 5$  **then**

            Assign  $\Delta\lambda := 1.5 \Delta\lambda$

**end if**

        Assign  $n_{\text{tot}} := n_{\text{tot}} + n_{\text{it}}$

        Assign  $n_{\text{inc}} = n_{\text{inc}} + 1$

        Assign  $n_{\text{it1}} := n_{\text{it}}$

**else**

*No or poor convergence of Newton-Raphson*

        Assign  $\lambda := \lambda - \Delta\lambda$

        Assign  $\Delta\lambda := 0.5 \Delta\lambda$

**end if**

**end while**

**return**  $(\mathbf{F}_h, \boldsymbol{\varphi}_h, \hat{\boldsymbol{\varphi}}_h, n_{\text{it}}, n_{\text{inc}})$

## Appendix B. Arc-Length Algorithm

---

**Algorithm 2** Arc-Length( $\mathbf{F}_h, \varphi_h, \hat{\varphi}_h, \lambda, \Delta l, \psi$ )

---

**Require:** Initialize  $\Delta\hat{\varphi}_h = 0$  ;  $\Delta\lambda = 0$

Compute  $(\mathbb{K}, R)$  from  $(\mathbf{F}_h, \varphi_h, \hat{\varphi}_h, \lambda P_{\max})$  using (23)-(25)

**while** residual > tol **do**

    Compute  $\delta\hat{\varphi}_h^R = \mathbb{K}^{-1}R$

    Compute  $\delta\hat{\varphi}_h^P = -\mathbb{K}^{-1}P_{\max}$

$\delta\lambda = \text{solve} [(\Delta\hat{\varphi}_h + \delta\hat{\varphi}_h^R + \delta\lambda\delta\hat{\varphi}_h^P)^2 + \psi^2(\lambda + \delta\lambda)^2 P_{\max}^2 = \Delta l^2]$

    Compute  $\delta\hat{\varphi}_h = \delta\hat{\varphi}_h^R + \delta\lambda\delta\hat{\varphi}_h^P$

    Assign  $\Delta\hat{\varphi}_h := \Delta\hat{\varphi}_h + \delta\hat{\varphi}_h$

    Assign  $\Delta\lambda := \Delta\lambda + \delta\lambda$

    Compute  $(\delta\mathbf{F}_h, \delta\varphi_h)$  from  $\delta\hat{\varphi}_h$  using (23)

    Assign  $(\mathbf{F}_h, \varphi_h, \hat{\varphi}_h) := (\mathbf{F}_h, \varphi_h, \hat{\varphi}_h) + (\delta\mathbf{F}_h, \delta\varphi_h, \delta\hat{\varphi}_h)$

    Compute  $(\mathbb{K}, R)$  from  $(\mathbf{F}_h, \varphi_h, \hat{\varphi}_h, \lambda P_{\max})$  using (23)-(25)

    Compute residual =  $\|R\|$

**end while**

**return**  $(\mathbf{F}_h, \varphi_h, \hat{\varphi}_h, \Delta\hat{\varphi}_h, \Delta\lambda)$

---



595 **Appendix C. Comparisons of several stabilization functions and solver**  
**metrics**

We present here some comparative data to assess the relative performance of the five stabilization functions mentioned in subsection 3.3.

Note that we tested a slightly different version of stabilization (17). Indeed, we instead implemented

$$\tau = \tau_0 - \frac{\beta}{L_c} \rho_{\min} \left( \frac{\partial \mathbf{F}_h}{\partial \mathbf{F}_h} \right) \quad (\text{C.1})$$

for the following reason. The original stabilization (17), presented for the DG method [51], makes use of a very small  $\tau_0$  (with  $\tau_0 = 0$  for most numerical examples) such that the scaling factor  $\beta$  essentially amplifies  $\rho_{\min}$ . This is however impossible in a HDG context since a minimum amount of stabilization is always required for the method to work, even when  $\rho_{\min} = 0$ . For our HDG method, a good estimation of  $\tau_0$  for moderate strains is given by (14), which is noticeably larger than  $\rho_{\min}$  for the applications considered in this paper. Therefore, it is more relevant to consider (C.1), where only  $\rho_{\min}$  is amplified by  $\beta$ , such that the contribution of  $\rho_{\min}$  to the stabilization can be isolated and assessed. When not specified, we use the default value  $\beta = 1$ .

In the following tables, we arbitrarily define the *slight locking* pathology as an underestimation of the displacements by less than 10% at maximum load. And we simply call *locking* the larger underestimations. When the loading algorithm 1 fails, the arc-length 2 is not expected to provide a more stable solution, except when the displacements are non-monotonic functions of the load, which happens only for the hinged roof case.

For the cantilever cases 5.2 and the slit plate 5.3.1, all the stabilization methods provide roughly the same amount of penalization since  $\nu = 0$  and the strains remain moderate. For the first cantilever problem 5.2.1, all stabilizations ensure the convergence of the algorithm 1 with  $n_{\text{inc}} = 10$  and  $n_{\text{tot}} = 65$ . For the second cantilever problem, some of the stabilizations lead to a slight locking pathology, as reported on table C.4. For the slit plate case, all the stabilizations work well with  $42 \leq n_{\text{inc}} \leq 53$ , and  $250 \leq n_{\text{tot}} \leq 270$  without any locking.

stabilization	$k$	mesh	$L_c$	$n_{inc}$	$n_{tot}$	reach $P_{max}$	notes
(14)	2	$16 \times 1$	1	23	678	✓	-
(14)	3	$8 \times 1$	1	141	1652	✓	-
(15)	2	$16 \times 1$	1	21	617	✓	slight locking
(15)	3	$8 \times 1$	1	123	1283	✓	slight locking
(16)	2	$16 \times 1$	1	22	652	✓	slight locking
(16)	3	$8 \times 1$	1	139	1635	✓	slight locking
(C.1)	2	$16 \times 1$	1	23	695	✓	-
(C.1)	3	$8 \times 1$	1	140	1633	✓	-
(19)	2	$16 \times 1$	1	23	609	✓	-
(19)	3	$8 \times 1$	1	141	1629	✓	-

Table C.4: Cantilever bent into a ring 5.2.2 - solver metrics for several stabilization functions. Here  $n_{max} = 50$  has been used for all cases.

The differences are more noticeable with the hemispheric shell, the pullout cylinder and the pinched cylinder cases, whose results are reported in tables C.5, C.6 and C.7 respectively. All these benchmarks have in common the concentration of large strains in localized areas (near the applied forces and wrinkles). Most stabilizations fail at some point, while (19) appears to work well. Interestingly, by using the minimum eigenvalue, the stabilization (C.1) may also work provided that the coefficient  $\beta$  is tuned. However,  $\beta$  appears to be case-dependent. If  $L_c$  is chosen too large for the pinched cylinder, the adaptive stabilization may still work, but the solution shows some strong spurious oscillations that require then the use of the arc-length algorithm 2.

The ringed roof 5.3.5, although having a very nonlinear response with respect to the load, involves only small strains. Therefore all the penalization functions perform equally well with  $n_{inc} = 54$  and  $n_{tot} = 108$  for the thick roof, and  $n_{inc} = 48$  and  $n_{tot} = 128$  for the thin roof. Note that these numbers largely depend on the choice of the user-defined characteristic length  $\Delta l$ .

stab.	$\beta$	$k$	mesh	$L_c$	$n_{inc}$	$n_{tot}$	reach $\mathcal{P}_{max}$	notes
(14)	-	2	$20 \times 20$	3	15	116		fails at $0.48 \mathcal{P}_{max}$
(14)	-	3	$8 \times 8$	3	26	181		fails at $0.88 \mathcal{P}_{max}$
(15)	-	2	$20 \times 20$	3	14	125		fails at $0.41 \mathcal{P}_{max}$
(15)	-	3	$8 \times 8$	3	29	209		fails at $0.89 \mathcal{P}_{max}$
(16)	-	2	$20 \times 20$	3	25	205		fails at $0.40 \mathcal{P}_{max}$
(16)	-	3	$8 \times 8$	3	31	289		fails at $0.35 \mathcal{P}_{max}$
(C.1)	1	2	$20 \times 20$	3	23	157		fails at $0.48 \mathcal{P}_{max}$
(C.1)	10	2	$20 \times 20$	3	28	177		fails at $0.56 \mathcal{P}_{max}$
(C.1)	100	2	$20 \times 20$	3	21	128	✓	-
(C.1)	1	3	$8 \times 8$	3	31	206		fails at $0.89 \mathcal{P}_{max}$
(C.1)	10	3	$8 \times 8$	3	31	189		fails at $0.89 \mathcal{P}_{max}$
(C.1)	100	3	$8 \times 8$	3	21	131	✓	-
(19)	-	2	$20 \times 20$	3	20	128	✓	-
(19)	-	3	$8 \times 8$	3	21	132	✓	-

Table C.5. Hemispherical shell case 5.3.2: solver metrics for several stabilization functions.

stab.	$\beta$	$k$	mesh	$L_c$	$n_{inc}$	$n_{tot}$	reach $P_{max}$	notes
(14)	-	2	$12 \times 18$	0.4	24	278		fails at $0.41 P_{max}$
(14)	-	3	$8 \times 12$	0.4	14	190		fails at $0.18 P_{max}$
(15)	-	2	$12 \times 18$	0.4	25	165		fails at $0.51 P_{max}$
(15)	-	3	$8 \times 12$	0.4	34	142		fails at $0.54 P_{max}$
(16)	-	2	$12 \times 18$	0.4	29	201		fails at $0.17 P_{max}$
(16)	-	3	$8 \times 12$	0.4	16	110		fails at $0.08 P_{max}$
(C.1)	1	2	$12 \times 18$	0.4	27	286		fails at $0.45 P_{max}$
(C.1)	10	2	$12 \times 18$	0.4	36	370		fails at $0.81 P_{max}$
(C.1)	100	2	$12 \times 18$	0.4	32	171	✓	-
(C.1)	1	3	$8 \times 12$	0.4	19	264		fails at $0.20 P_{max}$
(C.1)	10	3	$8 \times 12$	0.4	42	529		fails at $0.67 P_{max}$
(C.1)	100	3	$8 \times 12$	0.4	35	212	✓	-
(19)	-	2	$12 \times 18$	0.4	26	227	✓	-
(19)	-	3	$8 \times 12$	0.4	38	255	✓	-

Table C.6 Pullout cylinder case 5.3.3: solver metrics for several stabilization functions. Here,  $\lambda_{init} = 0.02$  has been used for all runs.

stab.	$\beta$	$k$	mesh	$L_c$	$n_{inc}$	$n_{tot}$	$\omega_{c0}$	$F_{max}$	notes
(14)	-	2	$48 \times 48$	0.25	34	802	1		fails at $0.35 P_{max}$
(14)	-	3	$24 \times 24$	0.25	31	770	1		fails at $0.16 P_{max}$
(15)	-	2	$48 \times 48$	0.25	53	955	1	✓	oscillatory, slight locking
(15)	-	3	$24 \times 24$	0.25	50	1023	1	✓	oscillatory, locking
(16)	-	2	$48 \times 48$	0.25	70	1138	1		fails at $0.18 P_{max}$
(16)	-	3	$24 \times 24$	0.25	63	761	1		fails at $0.15 P_{max}$
(C.1)	1	2	$48 \times 48$	0.25	40	540	1		fails at $0.76 P_{max}$
(C.1)	10	2	$48 \times 48$	0.25	68	601	1	✓	-
(C.1)	100	2	$48 \times 48$	0.25	64	557	1	✓	-
(C.1)	1	3	$24 \times 24$	0.25	23	644	1		fails at $0.20 P_{max}$
(C.1)	10	3	$24 \times 24$	0.25	156	2474	1		fails at $0.74 P_{max}$
(C.1)	100	3	$24 \times 24$	0.25	178	1895	1	✓	oscillatory
(19)	-	2	$48 \times 48$	0.25	50	468	1	✓	-
(19)	-	3	$24 \times 24$	0.25	50	1056	1	✓	-
(19)	-	2	$48 \times 48$	0.50	48	573	2	✓	oscillatory

Table C.7: Pinned cylinder case 5.3.4: solver metrics for several stabilization functions. Here,  $n_{max} = 50$  and  $\epsilon = 0.02$  have been used for all runs. In the notes column, *oscillatory* means that the mode develops some mesh-dependent non-physical oscillatory pattern.

## References

- 1  
2  
3  
4  
5  
6  
7  
8  
9
- 10
- 11 [1] B. Cockburn, G. E. Karniadakis, C.-W. Shu, The development of discontinuous galerkin methods, in: *Discontinuous Galerkin Methods*, Springer, 12 2000, pp. 3–50.
- 13  
14  
15  
16  
17 [2] G. E. Karniadakis, C.-W. Shu, B. Cockburn, *Discontinuous Galerkin Methods: Theory, Computation and Applications*, Springer, 2000.
- 18  
19  
20  
21 [3] J. S. Hesthaven, T. Warburton, *Nodal discontinuous Galerkin methods: algorithms, analysis, and applications*, Springer Science & Business Media, 22 2007.
- 23  
24  
25  
26 [4] B. Cockburn, D. Schötzau, J. Wang, Discontinuous galerkin methods for 27 incompressible elastic materials, *Computer methods in applied mechanics and engineering* 195 (25) (2006) 3184–3204.
- 28  
29  
30  
31 [5] A. Ten Eyck, A. Lew, Discontinuous galerkin methods for non-linear elasticity, *International Journal for Numerical Methods in Engineering* 67 (9) 32 (2006) 1204–1243.
- 33  
34  
35  
36  
37 [6] L. Noels, R. Radovitzky, A general discontinuous galerkin method for finite hyperelasticity: formulation and numerical applications, *International 38 Journal for Numerical Methods in Engineering* 68 (1) (2006) 64–97.
- 39  
40  
41  
42 [7] L. Noels, R. Radovitzky, Alternative approaches for the derivation of discontinuous galerkin methods for nonlinear mechanics, *Journal of Applied 43 Mechanics* 74 (5) (2007) 1031–1036.
- 44  
45  
46  
47  
48 [8] I. Djoko, F. Ebobisse, A. McBride, B. Reddy, A discontinuous galerkin 49 formulation for classical and gradient plasticity—part 1: Formulation and analysis, *Computer methods in applied mechanics and engineering* 196 (37) 50 (2007) 3881–3897.
- 51  
52  
53  
54  
55 [9] L. Noels, R. Radovitzky, An explicit discontinuous galerkin method for non-linear solid dynamics: Formulation, parallel implementation and scalability 56  
57  
58  
59  
60  
61  
62  
63  
64  
65

- 1  
2  
3  
4  
5  
6  
7  
8  
9 properties, *International Journal for Numerical Methods in Engineering*  
10 74 (9) (2008) 1393–1420.
- 11  
12 [10] S.-C. Soon, B. Cockburn, H. K. Stolarski, A hybridizable discontinuous  
13 Galerkin method for linear elasticity, *International journal for numerical*  
14 *methods in engineering* 80 (8) (2009) 1058–1092.
- 15  
16  
17  
18 [11] N. C. Nguyen, J. Peraire, Hybridizable discontinuous galerkin methods for  
19 partial differential equations in continuum mechanics, *Journal of Compu-*  
20 *tational Physics* 231 (18) (2012) 5955–5988.
- 21  
22  
23 [12] B. Cockburn, K. Shi, Superconvergent HDG methods for linear elasticity  
24 with weakly symmetric stresses, *IMA Journal of Numerical Analysis* 33 (3)  
25  
26  
27 (2013) 747–770.
- 28  
29 [13] G. Fu, B. Cockburn, H. Stolarski, Analysis of an hdg method for linear elas-  
30 ticity, *International Journal of Numerical Methods in Engineering* 102 (3-  
31  
32  
33  
34  
35  
36  
37  
38  
39  
40  
41  
42  
43  
44  
45  
46  
47  
48  
49  
50  
51  
52  
53  
54  
55  
56  
57  
58  
59  
60  
61  
62  
63  
64  
65
- 670 [14] W. Qiu, J. Shen, K. Shi, A hdg method for linear elasticity with strong  
symmetric stresses, *Mathematics of Computation* 87 (309) (2018) 69–93.
- [15] S. Soon, Hybridizable discontinuous galerkin method for solid mechanics,  
Ph.D. thesis, University of Minnesota (2008).
- [16] H. Kabaila, A. J. Lew, B. Cockburn, A hybridizable discontinuous galerkin  
680 formulation for non-linear elasticity, *Computer Methods in Applied Me-*  
*chanics and Engineering* 283 (2015) 303–329.
- [17] J. Shen, Hybridizable discontinuous galerkin methods for nonlinear elastic-  
ity, Ph.D. thesis, University of Minnesota (2017).
- [18] B. Cockburn, J. Shen, An algorithm for stabilizing hybridizable discontin-  
685  
ous galerkin methods for nonlinear elasticity, *Results in Applied Mathe-*  
*matics* (2019) 100001.

- 1  
2  
3  
4  
5  
6  
7  
8  
9 [19] T. Belytschko, A review of recent developments in plate and shell elements,  
10 Computational mechanics- Advances and trends (1986) 211–231.  
11  
12 [20] H. Stolarski, T. Belytschko, S.-H. Lee, A review of shell finite elements  
13 and corotational theories, Computational mechanics advances 2 (2) (1995)  
14 695 125–212.  
15  
16 [21] H. T. Yang, S. Saigal, A. Masud, R. Karania, A survey of recent shell  
17 finite elements, International Journal for numerical methods in engineering  
18 47 (1-3) (2000) 101–127.  
19  
20 [22] S. Güzey, H. Stolarski, B. Cockburn, S. Iyengar, Design and development of  
21 a discontinuous galerkin method for shells, Computer Methods in Applied  
22 Mechanics and Engineering 195 (20) (2006) 3528–3548.  
23  
24 [23] S. Güzey, B. Cockburn, H. Stolarski, The embedded discontinuous galerkin  
25 method: application to linear shell problems, International journal for nu-  
26 merical methods in engineering 70 (7) (2007) 757–790.  
27  
28 [24] L. Noels, A discontinuous galerkin formulation of non-linear kirchhoff-love  
29 shells, International journal for numerical methods in engineering 78 (3)  
30 (2009) 296–325.  
31  
32 [25] A. Ibrahimbegovic, R. L. Taylor, On the role of frame-invariance in struc-  
33 tural mechanics models at finite rotations, Computer Methods in Applied  
34 Mechanics and Engineering 191 (45) (2002) 5159–5176.  
35  
36 [26] S. Klinkel, J. Gruttmann, W. Wagner, A robust non-linear solid shell el-  
37 element based on a mixed variational formulation, Computer methods in  
38 applied mechanics and engineering 195 (1) (2006) 179–201.  
39  
40 [27] K. Ise, L. Yao, A hybrid stress and solid-shell element and its generaliza-  
41 tion for smart structure modelling. part i solid-shell element formulation,  
42 International Journal for Numerical Methods in Engineering 48 (4) (2000)  
43 545–564.  
44  
45  
46  
47  
48  
49  
50  
51  
52  
53  
54  
55  
56  
57  
58  
59  
60  
61  
62  
63  
64  
65



- 1  
2  
3  
4  
5  
6  
7  
8  
9  
10 [28] R. Hauptmann, K. Schweizerhof, A systematic development of solid-  
11 720 shell element formulations for linear and non-linear analyses employing  
12 only displacement degrees of freedom, *International Journal for Numerical*  
13 *Methods in Engineering* 42 (1) (1998) 49–69.  
14  
15  
16 [29] R. J. Alves de Sousa, R. P. Cardoso, R. A. F. F. Valente, J.-W. Yoon,  
17 J. J. Grácio, R. M. Natal Jorge, A new one-point quadrature enhanced  
18 725 assumed strain (eas) solid-shell element with multiple integration points  
19 along thicknesspart ii: nonlinear applications, *International Journal for*  
20 *Numerical Methods in Engineering* 67 (2) (2006) 160–188.  
21  
22  
23 [30] M. Jabareen, E. Mtnes, A solid-shell cosserat point element (sscp) for  
24 elastic thin structures at finite deformation, *Computational Mechanics*  
25 58 (1) (2016) 59–89.  
26 730  
27  
28 [31] O. Zienkiewicz, R. Taylor, *et al.*, A reduced integration technique in general  
29 analysis of plates and shells, *International Journal for Numerical Methods*  
30 *in Engineering* 3 (2) (1971) 275–290.  
31  
32  
33 [32] W. K. Liu, Y. Guo, S. Tang, T. Belytschko, A multiple-quadrature eight-  
34 node hexahedral finite element for large deformation elastoplastic analysis,  
35 735 *Computer Methods in Applied Mechanics and Engineering* 154 (1-2) (1998)  
36 69–132.  
37  
38  
39 [33] T. Belytschko, W. K. Liu, B. Moran, K. Elkhodary, *Nonlinear finite ele-*  
40 *ments for continua and structures*, John wiley & sons, 2013.  
41  
42  
43 [34] T. J. Hughes, Generalization of selective integration procedures to  
44 740 anisotropic and nonlinear media, *International Journal for Numerical Meth-*  
45 *ods in Engineering* 15 (9) (1980) 1413–1418.  
46  
47  
48 [35] T. J. Hughes, *The finite element method: linear static and dynamic finite*  
49 *element analysis*, Courier Corporation, 2012.  
50  
51  
52  
53  
54  
55  
56  
57  
58  
59  
60  
61  
62  
63  
64  
65

- 1  
2  
3  
4  
5  
6  
7  
8  
9  
10  
11  
12  
13  
14  
15  
16  
17  
18  
19  
20  
21  
22  
23  
24  
25  
26  
27  
28  
29  
30  
31  
32  
33  
34  
35  
36  
37  
38  
39  
40  
41  
42  
43  
44  
45  
46  
47  
48  
49  
50  
51  
52  
53  
54  
55  
56  
57  
58  
59  
60  
61  
62  
63  
64  
65
- 745 [36] J. C. Simo, M. Rifai, A class of mixed assumed strain methods and the method of incompatible modes, *International journal for numerical methods in engineering* 29 (8) (1990) 1595–1638.
- [37] R. Hauptmann, S. Doll, M. Harnau, K. Schweizer, of, ‘solid-shell’ elements with linear and quadratic shape functions at large deformations with nearly incompressible materials, *Computers & Structures* 79 (18) (2001) 1671 – 1685. doi:[https://doi.org/10.1016/S0045-7949\(01\)00103-1](https://doi.org/10.1016/S0045-7949(01)00103-1). URL <http://www.sciencedirect.com/science/article/pii/S0045794901001031>
- 755 [38] R. J. Alves de Sousa, R. P. Cardoso, R. A. Fontes Valente, J.-W. Yoon, J. J. Grácio, R. M. Natal Jorge, A new one-point quadrature enhanced assumed strain (eas) solid-shell element with multiple integration points along thickness: Part I geometrically linear applications, *International journal for numerical methods in engineering* 62 (7) (2005) 952–977.
- [39] R. P. Cardoso, J. V. Yoon, M. Mahardika, S. Choudhry, R. Alves de Sousa, R. Fontes Valente, Enhanced assumed strain (eas) and assumed natural strain (ans) methods for one-point quadrature solid-shell elements, *International Journal for Numerical Methods in Engineering* 75 (2) (2008) 156–187.
- 765 [40] K. Rah-W. van Paepegem, A.-M. Habraken, J. Degrieck, R. A. de Sousa, R. A. Valente, Optimal low-order fully integrated solid-shell elements, *Computational Mechanics* 51 (3) (2013) 309–326.
- [41] F. J. Hughes, T. Tezduyar, Finite elements based upon mindlin plate theory with particular reference to the four-node bilinear isoparametric element, *Journal of applied mechanics* 48 (3) (1981) 587–596.
- [42] E. N. Dvorkin, K.-J. Bathe, A continuum mechanics based four-node shell element for general non-linear analysis, *Engineering computations* 1 (1) (1984) 77–88.

- 1  
2  
3  
4  
5  
6  
7  
8  
9  
10 [43] L. Vu-Quoc, X. Tan, Optimal solid shells for non-linear analyses of multi-  
11 layer composites. i. statics, *Computer methods in applied mechanics and*  
12 *engineering* 192 (9-10) (2003) 975–1016.  
13  
14 [44] M. Suri, I. Babuška, C. Schwab, Locking effects in the finite element ap-  
15 proximation of plate models, *Mathematics of Computation* 64 (210) (1995)  
16 461–482.  
17  
18 [45] H. Hakula, Y. Leino, J. Pitkäranta, Scale resolution, locking, and high-  
19 order finite element modelling of shells. *Computer methods in applied me-*  
20 *chanics and engineering* 133 (3-4) (1996) 157–182.  
21  
22 [46] Y. Başar, U. Hanskötter, C. Schwab, A general high-order finite element  
23 formulation for shells at large strains and finite rotations, *International*  
24 *Journal for Numerical Methods in Engineering* 57 (15) (2003) 2147–2175.  
25  
26 [47] F. Celiker, B. Cockburn, H. K. Stolarski, Locking-free optimal discontinu-  
27 ous galerkin methods for timoshenko beams, *SIAM Journal on Numerical*  
28 *Analysis* 44 (6) (2006) 2297–2325.  
29  
30 [48] B. Cockburn, J. Gopalakrishnan, R. Lazarov, Unified hybridization of dis-  
31 continuous galerkin mixed, and continuous galerkin methods for second  
32 order elliptic problems, *SIAM Journal on Numerical Analysis* 47 (2) (2009)  
33 1319–1365.  
34  
35 [49] N. C. Nguyen, J. Peraire, B. Cockburn, High-order implicit hybridizable  
36 discontinuous Galerkin methods for acoustics and elastodynamics, *Journal*  
37 *of Computational Physics* 230 (10) (2011) 3695–3718.  
38  
39 [50] J. Bonet, A. J. Gil, R. D. Wood, *Nonlinear solid mechanics for finite element*  
40 *analysis: statics*, Cambridge University Press, 2016.  
41  
42 [51] A. Fen Eyck, F. Celiker, A. Lew, Adaptive stabilization of discontinuous  
43 galerkin methods for nonlinear elasticity: Motivation, formulation, and  
44 numerical examples, *Computer Methods in Applied Mechanics and Engi-*  
45 *neering* 197 (45-48) (2008) 3605–3622.  
46  
47  
48  
49  
50  
51  
52  
53  
54  
55  
56  
57  
58  
59  
60  
61  
62  
63  
64  
65

- 1  
2  
3  
4  
5  
6  
7  
8  
9 [52] A. Ten Eyck, F. Celiker, A. Lew, Adaptive stabilization of discontinuous  
10 galerkin methods for nonlinear elasticity: analytical estimates, *Computer*  
11 *Methods in Applied Mechanics and Engineering* 197 (2008) 2989–  
12 3000.  
13  
14  
15  
16 805 [53] P. Fernandez, A. Christophe, S. Terrana, N.-C. Nguyen, J. Peraire,  
17 Hybridized discontinuous galerkin methods for wave propagation, arXiv  
18 preprint arXiv:1807.00086.  
19  
20  
21 [54] D. Systèmes, *Abaqus analysis users manual*, Simulia Corp. Providence, RI,  
22 USA.  
23  
24  
25 810 [55] E. Riks, An incremental approach to the solution of snapping and buckling  
26 problems, *International Journal of Solids and Structures* 15 (7) (1979) 529–  
27 551.  
28  
29  
30 [56] M. Crisfield, A fast incremental/iterative solution procedure that handles  
31 snap-through, *Computers & Structures* 13 (1-3) (1981) 55–62.  
32  
33  
34 815 [57] D. Systèmes, *Abaqus theory manual*, Simulia Corp. Providence, RI, USA.  
35  
36 [58] G. Horrigmoe, P. G. Bergan, Nonlinear analysis of free-form shells by flat  
37 finite elements, *Computer Methods in Applied Mechanics and Engineering*  
38 16 (1) (1978) 11–35.  
39  
40  
41 [59] A. Saleeb, T. Chang, W. Graf, S. Yingyeunyong, A hybrid/mixed model  
42 for non-linear shell analysis and its applications to large-rotation problems,  
43 820 *International Journal for Numerical Methods in Engineering* 29 (2) (1990)  
44 407–440.  
45  
46  
47  
48 [60] K. Sze, L. Liu, S. Lo, Popular benchmark problems for geometric nonlinear  
49 analysis of shells, *Finite elements in analysis and design* 40 (11) (2004)  
50 1551–1569.  
51 825  
52  
53 [61] R. H. Macneal, R. L. Harder, A proposed standard set of problems to test  
54 finite element accuracy, *Finite elements in analysis and design* 1 (1) (1985)  
55 3–20.  
56  
57  
58  
59  
60  
61  
62  
63  
64  
65

- 1  
2  
3  
4  
5  
6  
7  
8  
9  
10 [62] J. Simo, D. Fox, M. Rifai, On a stress resultant geometrically exact shell  
11 830 model. part ii: The linear theory; computational aspects, *Computer Meth-*  
12 *ods in Applied Mechanics and Engineering* 73 (1) (1989) 83–92.
- 13  
14 [63] R. Hauptmann, K. Schweizerhof, S. Doll, Extension of the solid-shell  
15 concept for application to large elastic and large elastoplastic deforma-  
16 tions, *International Journal for Numerical Methods in Engineering*  
17 49 (9) 1121–1141. doi:10.1002/1097-0207(20001130)49:9<1121::  
18 835 AID-NME130>3.0.CO;2-F.  
19 URL [https://onlinelibrary.wiley.com/doi/abs/10.1002/  
20 1097-0207%2820001130%2949%3A9%3C1121%3A%3AAID-NME130%3E3.  
21 0.CO%3B2-F](https://onlinelibrary.wiley.com/doi/abs/10.1002/1097-0207%2820001130%2949%3A9%3C1121%3A%3AAID-NME130%3E3.0.CO%3B2-F)
- 22  
23  
24  
25  
26  
27 [64] M. W. Heinstein, J. D. Hales, W. L. Previk, S. W. Key, Summary compi-  
28 840 lation of shell element performance versus formulation., Tech. rep., Sandia  
29 National Laboratories (2011).
- 30  
31  
32 [65] A. Sabir, A. Lock, The applications of finite elements to large deflection  
33 geometrically nonlinear behaviour of cylindrical shells.
- 34  
35  
36 [66] P. Fernandez, N. C. Nguyen, J. Peraire, The hybridized discontinuous  
37 845 galerkin method for implicit large-eddy simulation of transitional turbu-  
38 lent flows. *Journal of Computational Physics* 336 (2017) 308–329.
- 39  
40  
41 [67] G. Kenway, G. Kennedy, J. Martins, Aerostructural optimization of the  
42 common research model configuration, in: 15th AIAA/ISSMO multidisci-  
43 plinary analysis and optimization conference, 2014, p. 3274.  
44  
45 850  
46  
47  
48  
49  
50  
51  
52  
53  
54  
55  
56  
57  
58  
59  
60  
61  
62  
63  
64  
65